



Strange Quarks and Parity Violation

K. S. KUMAR

Department of Physics, University of Massachusetts, Amherst, MA 01003, USA

and

P. A. SOUDER

Department of Physics, Syracuse University, Syracuse, NY 13244, USA

Abstract

We report on the study of parity violation in the scattering of polarized electrons to probe the contribution of strange quarks to the elastic nucleon form factors. We review the theoretical assumptions that are involved in isolating the strange form factors as well as the predictions for the size of the strange form factors. The experiments require the measurement of small asymmetries, typically $\leq 10^{-5}$. We describe in detail the general experimental techniques that are used to obtain this level of precision. Finally, we summarize specific experiments that have been published recently as well as new experiments in progress.

1 Introduction

1.1 Brief History

The proton is a state of three valence quarks bound by the strong forces of QCD. The QCD forces generate a “sea” of gluons, antiquarks, and even strange quarks inside the proton. One of the important open questions in the field is the role of the sea in the fundamental properties of the nucleon. Data on spin-dependent structure functions by the EMC collaboration published in 1988 [1] indicated that little of the spin of the proton is carried by the valence quarks. Prime candidates for the missing spin are sea quarks, gluons, and orbital angular momentum. Moreover, the EMC data suggested that significant spin is carried by the strange quarks.

The EMC result inspired a flurry of theoretical activity aimed at achieving a better understanding of the sea. One important idea, suggested by Kaplan and Manohar [2], was that strange quarks might also contribute to the magnetic moment and charge radius of the proton. In other words, strange quarks might have a significant contribution to the vector matrix elements in the nucleon. They pointed out that measurements of the weak neutral current amplitude in lepton-nucleon scattering might help isolate these form factors.

One clean way to access strange vector matrix elements via measurements of the weak neutral current amplitude is by studying parity violation in polarized electron scattering [3, 4, 5]. During the past decade, six experiments in three different laboratories have been initiated to use parity violation in polarized electron scattering to measure the strange vector matrix elements. Results from two of the experiments has been published, and additional data should become available over the next five years. This work is the subject of our review.

1.2 Strangeness in the Proton

Strange quarks can in principle contribute to the mass, momentum, spin, magnetic moment, and charge radius of the nucleon. In addition, strange quarks can increase the yield of strange mesons in inelastic scattering. The most firmly established effect of strange quarks in the proton is a contribution to the proton's momentum as established by charm production in deep inelastic neutrino scattering [6]. From that data, it is clear that the strange quarks carry a relatively small fraction, about $\sim 3\%$ [7] of the momentum of the proton at a scale of $Q^2 \sim 2 \text{ (GeV/c)}^2$.

The contribution of strange quarks to the mass of the proton arises from the matrix element $\langle P | \bar{s}s | P \rangle$. The value may be inferred from the “sigma term” in $\pi - N$ scattering. The result is that strange quarks contribute about 10% of the mass [8]. However, significant uncertainty in this estimate arises from problems with both the data and the extensive theory required to interpret the result.

Another suggestive piece of empirical evidence is OZI violations in $\bar{p}p$ annihilations. Certain decays involving ϕ mesons are measured to be strongly enhanced compared to naive predictions. One of several explanations is that the Fock-space decomposition of the proton wave function has a sizable polarized $\bar{s}s$ component [9].

The contribution of strange quarks to the spin of the proton may be inferred from the first moment Γ_1 of the spin structure functions $g_1(x)$ for the proton and neutron. Indeed, much of the interest in the role of the strange quarks in the proton was generated by spin structure function data published by the EMC collaboration in 1988. Considerable progress has been made in this field in the past decade. An impressive amount of data have been obtained with increased precision in several laboratories, and next-to-leading order QCD analyses have been performed by several groups [10, 11, 12, 13]. The contribution of the strange quarks Δs to the net spin of the proton in units of $\hbar/2$ is about -0.1 [14], where $2(\Delta s)s_\mu \equiv \langle P | \bar{s}\gamma_\mu\gamma_5 s | P \rangle$. As stated is Ref. [14], the error on $\Delta s \sim 0.05$, where the uncertainty arises from various theoretical issues including especially $SU(3)_f$ symmetry breaking.

The spin-structure function data also indicate that the fraction of the proton spin carried by all of the quarks is $\Delta\Sigma \sim 0.3$, much smaller than predicted by naive models. Depending on the analysis and the precise definition, the range of values of $\Delta\Sigma$ deduced from experiment varies by ± 0.1 . This fact is relevant since one candidate for some of the “missing” spin is the sea quarks, and if the sea quarks are polarized, it is reasonable that the strange quarks would be polarized.

In summary, the above phenomena suggest that $\bar{s}s$ pairs may play a significant role in many aspects of the proton. It is important to establish as many effects of strangeness as possible in a convincing way.

1.3 Elastic Electroweak Scattering

Parity violation in the scattering of polarized electrons from various nuclei provides another observable that is sensitive to the presence of strange quarks in the proton [3, 4, 5]. The dominant sensitivity is to the matrix element $\langle p | \bar{s}\gamma_\mu s | p \rangle$, which is not directly related to any of the phenomena discussed in the

previous section. This matrix element contains information on the strange contribution to the charge radius and magnetic moment of the proton.

The interpretation of the parity-violating asymmetry in terms of strangeness is relatively clean. The main assumption is charge symmetry. Also required is the accurate knowledge of both proton and neutron electromagnetic form factors, a subject of considerable interest in itself. The status of this field and implications for strange form factors is discussed in Section 3.2 below. Another relevant issue, which has recently received much attention, is the radiative corrections to the axial nucleon current (see Section 3.3).

There is no reliable theoretical estimate of how large the matrix element $\langle p | \bar{s} \gamma_\mu s | p \rangle$ is, but there are models, among those discussed in Sec. 3.1 below, that suggest that the effects of strange quarks may be significant. If indeed the effects are as large as some of the models suggest, planned experiments have the sensitivity to establish the presence of strange form factors.

2 Phenomenology of Elastic Electron Scattering

2.1 Introduction

Parity violation in the scattering of polarized electrons arises from the simple fact that the weak interaction of an electron with a target particle depends upon its helicity. In this section, we introduce the formalism for a quantitative discussion of parity violating electron scattering experiments. We begin with the case of potential scattering, where the theory is most transparent. Potential scattering is a reasonable approximation for the practical case of scattering from a spinless, isoscalar target such as ^{12}C or ^4He .

We will then discuss elastic scattering from the proton. The results are more complicated because the non-zero proton spin gives rise to several form factors as opposed to the single form factor required to describe isoscalar, spinless nuclei. This is presently the case for which the most experimental effort is devoted. Finally, we will give the results for other relevant processes: the neutron, quasielastic scattering from the deuteron, and ^4He .

2.2 Potential Scattering

We start with potential scattering in the Born approximation. The target is a spinless potential distribution fixed in space while the electron is treated ultra-relativistically. To fix our notation, we first discuss purely electromagnetic scattering. Consider an electron of energy E scattered by an angle θ with momentum transfer $q = 2E \sin(\theta/2)$. The potential corresponds to a spatial charge distribution $\rho(r)$ which is the Fourier transform of the electromagnetic form factor

$$F(q) = \int d^3r \rho(r) \exp[i\mathbf{q} \cdot \mathbf{r}]. \quad (1)$$

The cross section is given by

$$\frac{d\sigma}{d\Omega} = |f(\theta)|^2 \cos^2(\theta/2), \quad (2)$$

where the scattering amplitude $f(\theta)$ may be written

$$f(\theta) = \frac{2\alpha}{q^2} F(q). \quad (3)$$

The scattering amplitude has two factors. The first is the form factor $F(q)$ which describes the spatial distribution of the charge. The second is $2\alpha/q^2$ which is the amplitude for scattering from a point distribution characterized by the following potential:

$$V(r) = \frac{e^2}{4\pi r}. \quad (4)$$

For weak scattering, the following potential may be used:

$$V(r) = k e^2 g^B g^T \frac{\exp[-Mr]}{4\pi r}, \quad (5)$$

where g^B is the weak charge of the incident beam particle and g^T is the weak charge of the target particle in units of the electron charge e . Also $k = (\sin \theta_W \cos \theta_W)^2$ is the strength of the coupling and M is the mass of the exchanged Z -boson.

One central feature of *longitudinally polarized* electron scattering is that the weak charge of a relativistic electron, and thus the cross section, depends on its helicity. Thus $g^R \neq g^L$, where $g^R(g^L)$ is the charge of an electron with right(left) helicity.

The other key feature of Table 1 is that the relative sizes of the weak and electromagnetic charges of the quarks are different. Since for this case we are using a spinless target, the vector charge g^V is the relevant weak charge for the quarks. The up quark has the strongest electromagnetic charge whereas the down and strange quarks have the strongest weak vector charge. The net result is that the charge distribution in an extended potential as seen by an electromagnetic probe might be quite different from the charge distribution seen by a weak probe of the same extended potential.

In discussing neutral weak amplitudes, it is sometimes more convenient to discuss vector and axial-vector weak charges, which are just linear combinations of the left- and right-handed weak charges: $g^R = g^V + g^A$ and $g^L = g^V - g^A$. The weak and electromagnetic charges of the electrons and relevant quarks are given in Table 1.

A convenient way to describe the charge distributions of the various quarks is to use a *number density* $\rho_i(r)$ for each quark flavor $i = u, d, s$ and a corresponding form factor

$$F_i(q) = \int d^3r \rho_i(r) \exp[i\mathbf{q} \cdot \mathbf{r}]. \quad (6)$$

To compute the resulting scattering amplitudes, we use the following potential form that is valid for both weak and electromagnetic interactions:

$$V_{ji}(r) = k_j e^2 g_{ji}^B g_j^T \frac{\exp[-M_j r]}{4\pi r}. \quad (7)$$

Here $j = \gamma(Z)$ denotes the electromagnetic(weak) interaction and again i denotes the quark flavor. For example, $M_j = 0$ and $k_j = 1$ for the electromagnetic interaction, and $M_j = M_Z$ for the neutral weak current.

The result is that all electromagnetic and weak scattering from a given potential may be described by the same three F_i . The scattering amplitude $f_{ji}(q)$ is given by the general form:

$$f_{ji}(q) = -\frac{1}{2\pi} \int V_{ji}(\mathbf{r}) \exp[i\mathbf{q} \cdot \mathbf{r}] d^3r = \frac{(2k_j \alpha g_j^B g_{ji}^T)}{(q^2 + M_j^2)} F_i(q). \quad (8)$$

As in the electromagnetic case, each scattering amplitude factors into two pieces. The first is a form factor F_i describing the spatial distribution of the quarks. It is independent of the interaction, and thus

Table 1: Electromagnetic and weak charges for the electron and light quarks. The helicity charges are given by $g^R = g^V + g^A$ and $g^L = g^V - g^A$.

Particle	q^{em}	g^V	g^A
e^-	-1	$-\frac{1}{4} + \sin^2 \theta_W$	$\frac{1}{4}$
u	$\frac{2}{3}$	$\frac{1}{4} - \frac{2}{3} \sin^2 \theta_W$	$-\frac{1}{4}$
d, s	$-\frac{1}{3}$	$-\frac{1}{4} + \frac{1}{3} \sin^2 \theta_W$	$\frac{1}{4}$

has no index j . The second piece is the factor describing the point-like interaction. The cross section is given by the coherent sum of all scattering amplitudes $f_{ji}(q)$

$$\frac{d\sigma}{d\Omega} = \sum_{ji} |f_{ji}(\theta)|^2 \cos^2(\theta/2). \quad (9)$$

The sum of amplitudes includes all quarks (i) contributing to the potential and both weak and electromagnetic interactions (j).

For ordinary electromagnetic scattering, $q \ll M_Z$, the weak interaction is negligible, and only one combination of the quark form factors survives:

$$F_\gamma = \sum g_i^{em} F_i = \frac{2}{3} F_u - \frac{1}{3} (F_d + F_s). \quad (10)$$

To experimentally isolate the contribution from each of the three flavors, measurements of weak scattering amplitudes are required, which we discuss next.

2.3 Parity Violation

The most practical way to measure the weak amplitude in electron scattering is to measure the asymmetry

$$A^{PV} = \frac{d\sigma_R - d\sigma_L}{d\sigma_R + d\sigma_L}. \quad (11)$$

If A^{PV} is non-zero, it constitutes parity violation and is dominated by the interference between the weak and electromagnetic amplitudes.

The cross section is proportional to the square of the scattering amplitudes:

$$f^R = f_\gamma + f_Z^R; \quad f^L = f_\gamma + f_Z^L, \quad (12)$$

where

$$f_\gamma(\theta) = -\frac{2\alpha}{q^2} \sum q_j^{em} F_j(q); \quad f_Z^{L(R)}(\theta) = \frac{2\alpha k_Z g^{L(R)}}{M_Z^2} \sum g_j^V F_j(q). \quad (13)$$

Here, $g^{L(R)}$ is the weak charge of the electron, g_i^V is the vector charge of the i th quark flavor, and $k_Z = (\sin \theta_W \cos \theta_W)^{-2}$. The asymmetry is

$$A^{PV} = \frac{|f^R|^2 - |f^L|^2}{|f^R|^2 + |f^L|^2} \simeq \frac{f_\gamma(f_Z^R - f_Z^L)}{f_\gamma^2} = \frac{f_Z^R - f_Z^L}{f_\gamma}. \quad (14)$$

This equation gives the essence of the parity-violating asymmetry. The weak-electromagnetic interference gives rise to a ratio of *amplitudes* rather than the ratio of the squares of the amplitudes. Since $g^R - g^L = 2g^A = 1/2$, we have

$$f_Z^R - f_Z^L = \frac{\alpha k_Z}{M_Z^2} \sum g_j^V F_j(q). \quad (15)$$

When the weak and electromagnetic charges for the quarks are included, we get:

$$\begin{aligned} A^{PV} &= -\frac{k_Z q^2 \sum g_j^V F_j}{2M_Z^2 \sum q_j F_j} \\ &= -\frac{k_Z q^2 \left(\frac{1}{4} - \frac{2}{3} \sin^2 \theta_W\right) F_u + \left(-\frac{1}{4} + \frac{1}{3} \sin^2 \theta_W\right) (F_d + F_s)}{2M_Z^2 \left(\frac{2}{3} F_u - \frac{1}{3} (F_d + F_s)\right)}. \end{aligned} \quad (16)$$

A measurement of A^{PV} thus provides one more combination of form factors such as that in Eqn. 10.

To isolate F_s , one more equation is needed. For a spinless $I = 0$ nucleus such as ${}^4\text{He}$ or ${}^{12}\text{C}$, the distribution of up and down quarks must be identical. For these cases, we have the equation

$$F_u = F_d \equiv F. \quad (17)$$

By combining this with Eqn. 16, we obtain:

$$\begin{aligned} A^{PV} &= -\frac{k_Z q^2}{2M_Z^2} \left(\frac{-\frac{1}{3} \sin^2 \theta_W (F - F_s) - \frac{1}{4} F_s}{\frac{1}{3} (F - F_s)} \right) \\ &= \frac{k_Z q^2}{2M_Z^2} \left(\sin^2 \theta_W + \frac{F_s}{4F_\gamma} \right), \end{aligned} \quad (18)$$

where F_γ is defined in Eqn. 10. Here the asymmetry is approximately proportional to the square of the momentum transfer, as is expected from the ratio of the propagators. This is a general feature of most reactions.

The above formula has two useful applications. The first is for low values of q . Since the net strangeness of nuclear matter is zero, Eqn. 6 implies that $F_s(0) = 0$. In this limit, Eqn. 18 is independent of hadronic structure, and can be used to precisely test the assumptions of the Standard Model [15, 16, 17]. On the other hand, for larger values of q , the asymmetry provides a clean measure of F_s [5, 18].

2.4 Nucleon Scattering

Extending the above method to relativistic nucleons is straightforward. Instead of the three-momentum transfer q , we use the space-like four-momentum transfer squared $Q^2 > 0$. An especially important feature of the nucleon is that it has spin 1/2, which gives rise to a magnetic form factor and also an axial vector form factor. The most general possible current for elastic electron nucleon scattering assuming current conservation, Lorentz invariance, and time reversal is

$$\begin{aligned} j_\mu^a(\text{nucleon}) &= \langle p(k', s') | j_\mu^a | p(k, s) \rangle = \\ &\bar{u}(k', s') [F_1^a(Q^2) \gamma_\mu + \frac{i}{2M} F_2^a(Q^2) \sigma_{\mu\nu} q^\nu + F_A^a(Q^2) \gamma_\mu \gamma^5 + F_P^a(Q^2) \gamma^5 q_\mu] u(k, s), \end{aligned} \quad (19)$$

where the F_i^a 's are Dirac vector form factors, F_A^a is the axial form factor, and F_P^a is the pseudoscalar form factor that plays no role in elastic scattering due to kinematic factors. All form factors are real and

depend only upon Q^2 . There are four currents, denoted by the superscript a , since the target particle can be a proton or a neutron and the current can be electromagnetic or weak.

Formulas for cross sections and asymmetries are usually expressed in terms of the Sachs form factors defined by:

$$G_E^a \equiv F_1^a - \tau F_2^a; \quad G_M^a \equiv F_1^a + F_2^a. \quad (20)$$

where $\tau = Q^2/4M^2$. The differential cross section for unpolarized electromagnetic electron scattering from the proton is then

$$\frac{d\sigma}{d\Omega}\bigg|_{lab} = \left(\frac{\alpha^2}{4E^2 \sin^4 \frac{\theta}{2}} \right) \frac{E'}{E} \left\{ \frac{(G_E^{p\gamma})^2 + \tau(G_M^{p\gamma})^2}{1 + \tau} \cos^2 \frac{\theta}{2} + 2\tau(G_M^{p\gamma})^2 \sin^2 \frac{\theta}{2} \right\}. \quad (21)$$

The neutron cross section is given by changing the superscript p to n .

The parity-violating electroweak asymmetry without radiative corrections is given by

$$A^{PV} = \frac{\sigma_R - \sigma_L}{\sigma_R + \sigma_L} = \left[\frac{-G_F Q^2}{\pi \alpha \sqrt{2}} \right] \quad (22)$$

$$\times \frac{\varepsilon G_E^{p\gamma} G_E^{pZ} + \tau G_M^{p\gamma} G_M^{pZ} - \frac{1}{2}(1 - 4 \sin^2 \theta_W) \varepsilon' G_M^{p\gamma} G_A^{pZ}}{\varepsilon (G_E^{p\gamma})^2 + \tau (G_M^{p\gamma})^2},$$

where $\varepsilon = [1 + 2(1 + \tau) \tan^2(\theta/2)]^{-1}$ is the transverse polarization of the virtual photon exchanged and $\varepsilon' = \sqrt{\tau(1 + \tau)(1 - \varepsilon^2)}$. An important feature of this result is that the asymmetry at backward angles involves the axial form factor G_A^{pZ} even though the target is unpolarized. The reason is that helicity is conserved, so that the relevant coupling at backward angles is $g_b^R g_t^R (g_b^L g_t^L)$ for right(left) handed electrons. Then the difference between the couplings of right- and left-handed electron $g_b^R g_t^R - g_b^L g_t^L = -2(g_b^V g_t^A + g_b^A g_t^V)$. This introduces an axial term and, as discussed below, the radiative corrections of this term are quite significant.

The above results involve many form factors. However, as for the case of potential scattering discussed above, we can relate all of the form factors to a few *flavor form factors* as follows:

$$\begin{aligned} \langle p | j_\mu^a | p \rangle &= \langle p | \sum g_i^{Va} \bar{u}_i \gamma_\mu u_i | p \rangle + \langle p | \sum g_i^{Aa} \bar{u}_i \gamma_\mu \gamma_5 u_i | p \rangle \\ &= \bar{u}_p \sum \left[g_i^{Va} (F_1^i \gamma_\mu + \frac{i}{2M} F_2^i \sigma_{\mu\nu} q^\nu) + g_i^{Aa} F_A^i \gamma_\mu \gamma_5 \right] u_p, \end{aligned} \quad (23)$$

where g_i^a is the coupling of the current by boson a to quark i . The spinor of the proton is denoted u_p , and the spinors of the quarks are denoted u_i . Thus the flavor form factors are defined:

$$\begin{aligned} \langle p | \bar{u}_i \gamma_\mu u_i | p \rangle &= \bar{u}_p (F_1^i \gamma_\mu + \frac{i}{2M} F_2^i \sigma_{\mu\nu} q^\nu) u_p \\ \langle p | \bar{u}_i \gamma_\mu \gamma_5 u_i | p \rangle &= \bar{u}_p F_A^i \gamma_\mu \gamma_5 u_p. \end{aligned} \quad (24)$$

There are a total of nine flavor form factors since there are three flavors times three Lorentz invariants:

$$\begin{aligned} F_1^u, \quad F_2^u, \quad F_A^u \\ F_1^d, \quad F_2^d, \quad F_A^d \\ F_1^s, \quad F_2^s, \quad F_A^s \end{aligned} \quad (25)$$

To include neutron scattering with the same set of form factors, we invoke charge symmetry:

$$p \rightarrow n \quad \Rightarrow \quad u \rightarrow d, \quad d \rightarrow u, \quad s \rightarrow s. \quad (26)$$

This implies the analog of Eqn. 17:

$$F_1^u \equiv F_1^{pu} = F_1^{nd}, \quad F_1^d \equiv F_1^{pd} = F_1^{nu}, \quad F_1^s \equiv F_1^{ps} = F_1^{ns}. \quad (27)$$

This is the analog of setting $F_u = F_d$ for the $I = 0$ case given above.

The weak and electromagnetic currents may be expressed in terms of these flavor form factors for the proton as follows. The electromagnetic current in term of quarks is

$$j_\mu^\gamma = \frac{2}{3} \bar{u} \gamma_\mu u - \frac{1}{3} \bar{d} \gamma_\mu d + \frac{2}{3} \bar{c} \gamma_\mu c - \frac{1}{3} \bar{s} \gamma_\mu s + \dots$$

Thus by Eqns. 23 and 27

$$F_i^{p\gamma} = \frac{2}{3} F_i^u - \frac{1}{3} F_i^d - \frac{1}{3} F_i^s; \quad F_i^{n\gamma} = \frac{2}{3} F_i^d - \frac{1}{3} F_i^u - \frac{1}{3} F_i^s. \quad (28)$$

Similarly for the weak current

$$\begin{aligned} j_\mu^Z &= \left(\frac{1}{4} - \frac{2}{3} \sin^2 \theta_W\right) \bar{u} \gamma_\mu u - \left(\frac{1}{4} - \frac{1}{3} \sin^2 \theta_W\right) \bar{d} \gamma_\mu d \\ &+ \left(\frac{1}{4} - \frac{2}{3} \sin^2 \theta_W\right) \bar{c} \gamma_\mu c - \left(\frac{1}{4} - \frac{1}{3} \sin^2 \theta_W\right) \bar{s} \gamma_\mu s \\ &- \frac{1}{4} \bar{u} \gamma_\mu \gamma_5 u + \frac{1}{4} \bar{d} \gamma_\mu \gamma_5 d - \frac{1}{4} \bar{c} \gamma_\mu \gamma_5 c + \frac{1}{4} \bar{s} \gamma_\mu \gamma_5 s. \end{aligned} \quad (29)$$

Consequently:

$$F_i^{pZ} = \left(\frac{1}{4} - \frac{2}{3} \sin^2 \theta_W\right) F_i^u - \left(\frac{1}{4} - \frac{1}{3} \sin^2 \theta_W\right) (F_i^d + F_i^s). \quad (30)$$

With Eqns. 28 and 30, elastic electron, neutrino, and antineutrino scattering and parity-violating electron scattering from either the proton and neutron can be described by the same set of form factors.

Any non-singular linear combination of the F_i^u , F_i^d , and F_i^s may be used for expressing cross sections and asymmetries. The best known form factors are G_E^γ and G_M^γ for the proton and neutron. Thus it is traditional to use $G_{E,M}^{p\gamma}$, $G_{E,M}^{n\gamma}$, and $G_{E,M}^s$ as the independent form factors. In terms of these quantities,

$$G_{E,M}^{pZ} = \frac{1}{4} (G_{E,M}^{p\gamma} - G_{E,M}^{n\gamma}) - \sin^2 \theta_W G_{E,M}^{p\gamma} - \frac{1}{4} G_{E,M}^s. \quad (31)$$

Also

$$G_A^{pZ} = -\frac{1}{2} G_A^{(1)} + \frac{1}{4} F_A^s. \quad (32)$$

where [19]

$$(F_A^u - F_A^d)/2 \equiv G_A^{(1)} = g_A G_A^D; \quad G_A^D = (1 + 3.32\tau)^{-2}. \quad (33)$$

is the isovector axial form factor. From beta decay of the neutron $g_A = 1.26$. Finally, $\Delta s \equiv F_A^s(0)/2$. The axial mass $M_A = 1.026 \pm 0.021$ [20] is obtained from neutrino scattering.

Using $G_{E,M}^{p\gamma}$, $G_{E,M}^{n\gamma}$, and $G_{E,M}^s$ as the three independent electric(magnetic) form factors is potentially deceptive in that it naively looks like electromagnetic scattering is independent of $G_{E,M}^s$. This is, of course, not true. However, it is true that with just electromagnetic scattering, it is impossible to isolate

the contribution from three different quark flavors. When Eqns. 31 and 32 are substituted into A^{PV} (Eqn. 22), the result depends on the electromagnetic proton and neutron form factors and the strange form factors. There is a firm prediction for A^{PV} if strangeness is neglected and if radiative corrections (see Section 3.3) are included. Any deviation of the measured asymmetry from the prediction could then be attributable to non-zero strange form factors.

The equation for extracting strange form factors from A^{PV} and electromagnetic scattering data, obtained by combining the results from Eqns. 22, 31, 32, is

$$A^{PV} = \left[\frac{-G_F M_p^2 \tau}{\pi \alpha \sqrt{2}} \right] \left\{ (1 - 4 \sin^2 \theta_W) - \frac{[\varepsilon G_E^{p\gamma}(G_E^{n\gamma} + G_E^s) + \tau G_M^{p\gamma}(G_M^{n\gamma} + G_M^s)]}{\varepsilon (G_E^{p\gamma})^2 + \tau (G_M^{p\gamma})^2} \right. \\ \left. \frac{(1 - 4 \sin^2 \theta_W) \sqrt{\tau(1 + \tau)} \sqrt{1 - \varepsilon^2 G_M^{p\gamma}(-G_A^{(1)} + \frac{1}{2} F_A^s)}}{\varepsilon (G_E^{p\gamma})^2 + \tau (G_M^{p\gamma})^2} \right\}. \quad (34)$$

This asymmetry is quite sensitive to G_E^s and G_M^s . Due to the factor of $(1 - 4 \sin^2 \theta_W)$, there is little sensitivity to F_A^s and thus Δs .

The contribution of the strange form factors to the asymmetry depends on the kinematics. For forward angles, where ε is large, the sensitivity to G_E^s is maximized. The contribution from G_M^s appears at all angles. Another interesting case is forward angles as $\tau \rightarrow 0$. Since $G_E^s(0) = 0$, the asymmetry becomes independent of strange form factors. Hence elastic scattering from hydrogen can serve as a test of the Standard Model [17], similar to the case for Eqn. 18.

It is tempting, but sloppy, to interpret G_E^s as the Fourier transform of the spatial distribution of strange quarks. The problem is that the nucleon recoils during the scattering, and when the nucleon recoils, G_E^s and G_M^s can mix in ways that depend upon unknown microscopic details of nucleon structure.

2.5 Neutrons, Deuterium, and ^4He

The above theory is straightforward to extend to the case of a neutron target. The result is:

$$A_n^{PV} = \left[\frac{-G_F M_p^2 \tau}{\pi \alpha \sqrt{2}} \right] \left\{ (1 - 4 \sin^2 \theta_W) - \frac{[\varepsilon G_E^{n\gamma}(G_E^{p\gamma} + G_E^s) + \tau G_M^{n\gamma}(G_M^{p\gamma} + G_M^s)]}{\varepsilon (G_E^{n\gamma})^2 + \tau (G_M^{n\gamma})^2} \right. \\ \left. \frac{(1 - 4 \sin^2 \theta_W) \sqrt{\tau(1 + \tau)} \sqrt{1 - \varepsilon^2 G_M^{n\gamma}(G_A^{(1)} + \frac{1}{2} F_A^s)}}{\varepsilon (G_E^{n\gamma})^2 + \tau (G_M^{n\gamma})^2} \right\}. \quad (35)$$

For quasi-elastic scattering from the deuteron in the impulse approximation, the asymmetry is just the weighted sum of the proton and neutron asymmetries:

$$A_d^{PV} = \frac{A_p^{PV} [\varepsilon (G_E^{p\gamma})^2 + \tau (G_M^{p\gamma})^2] + A_n^{PV} [\varepsilon (G_E^{n\gamma})^2 + \tau (G_M^{n\gamma})^2]}{[\varepsilon (G_E^{p\gamma})^2 + \tau (G_M^{p\gamma})^2] + [\varepsilon (G_E^{n\gamma})^2 + \tau (G_M^{n\gamma})^2]}. \quad (36)$$

The possible corrections to the above formula are discussed in the literature [21, 22]. The importance of the deuteron is that the asymmetry is much less sensitive to G_M^s . Thus, in the backward direction

the dominant isovector part of the axial proton current can be isolated. For forward scattering, G_E^s dominates.

Scattering off a spinless, isoscalar nucleus completely eliminates the axial current as well as G_M^s . The asymmetry is [5, 18]

$$A^{PV} = \frac{G_F Q^2}{\pi \alpha \sqrt{2}} \left[\sin^2 \theta_W + \frac{G_E^s}{2(G_E^p + G_E^n)} \right]. \quad (37)$$

This expression follows from Eqn. 18 with the additional assumptions that the nuclear form factors are a product of the nucleon form factor times another form factor arising from the shape of the nucleus. Practical spinless isoscalar targets include ^4He and ^{12}C .

3 Predictions and Interpretation

3.1 Theoretical Estimates of Strange Form Factors

In designing experiments, it is helpful to have theoretical guidance as to the size of effects predicted. In the case of searching for non-zero strange form factors, there are many key questions. For example, should one look for G_E^s , G_M^s , or G_A^s ? At what Q^2 should the experiment be done?

There is a vast literature on the subject of computing strange form factors. Many different techniques are used [23, 24, 25, 26, 27, 28, 29, 30, 31, 32, 33, 34, 35, 36]. Unfortunately, the problem is one in non-perturbative QCD since $m_s \sim \Lambda_{QCD}$, and reliable techniques for attacking this problem have not yet been developed. Much has been learned, and we may hope that realistic calculations will become feasible. Even if this goal proves elusive, the calculations are significant since:

- The fact that strange form factors may be computed by so many techniques attests to the physical significance of the issue.
- For better or worse, typical results of the calculations have been used to justify various experiments.

Numerous choices of degrees of freedom have been made in attacking this problem. One choice is the bare quarks, which can only be used in lattice calculations. Models with meson degrees of freedom are popular and make physical sense, but suffer from the problem that the result changes significantly as additional features are incorporated. The Skyrme model and the Nambu-Jona-Lasino model are other approaches.

A summary of predictions is given in Table 2. Most of the calculations are done at $\tau = 0$, where the following definitions apply

$$\mu_s = G_M^s(0); \quad \rho_s \equiv \left. \frac{dG_E^s}{d\tau} \right|_{\tau=0}. \quad (38)$$

Another common parameter is the strange charge radius

$$\langle r_s^2 \rangle = -6 \left. \frac{dF_1^s}{dQ^2} \right|_{Q^2=0}; \quad \rho_s = -\frac{2}{3} M_p^2 \langle r_s^2 \rangle - \mu_s.$$

Due to the recoil of the proton, one must be careful about how the charge radius is interpreted [37].

From the table, we see that there are approximately two clusters of predictions for μ_s . One cluster is at ~ -0.3 . This is about 10% of μ_p , and is reminiscent of values of $\Delta s \sim -0.1$. The establishment of a value that large would clearly be striking. The other cluster has μ_s at the less surprising level of a

Table 2: Some published theoretical estimates for ρ_s and μ_s .

Method	ρ_s	μ_s	Author
Pole fits	-2.1 ± 1.0	-0.31 ± 0.09	Jaffe [23]
	-2.9 ± 0.5	-0.24 ± 0.03	Hammer [24]
Kaon Loops	0.2	-0.03	Koepf [25]
	0.5 ± 0.1	-0.35 ± 0.05	Ramsey-Mulolf [26]
	0.3	-0.12	Ito [27]
Unquenched Quarks	0.6	0.04	Geiger [28]
Meson Exchange	0.03	0.002	Meissner [29]
Meson Cloud	–	0.0066	Ma [30]
NJL	3.0 ± 0.08	-0.15 ± 0.10	Weigel [31]
Skyrme	1.6	-0.13	Park [32]
	-0.7	-0.05	Park [33]
Chiral Bag Model	–	0.37	Hong [34]
Lattice QCD	1.7 ± 0.7	-0.36 ± 0.20	Dong [35]
Dispersion Relations	0.99	-0.42	Hammer [36]

few percent of μ_p . For the strangeness radius, there is little consensus on the *sign* of ρ_s . However, there are again two clusters, one with $|\rho_s| \sim 2$ and one with $|\rho_s|$ at least an order of magnitude smaller. This may be compared with $\rho_p \equiv dG_E^p/d\tau \sim 10$. Again, 10% effects can be generated by models.

Another issue is the Q^2 or τ dependence of the strange form factors. A convenient way to describe this, inspired by the Galster parameterization [38] of $G_E^n(Q^2)$, is to introduce new parameters λ_E^s and λ_M^s as suggested in the review by Musolf et al. [19]:

$$G_E^s = \frac{\rho_s \tau G_E^p}{1 + \lambda_E^s \tau}; \quad G_M^s = \frac{\mu_s G_E^p}{1 + \lambda_M^s \tau}. \quad (39)$$

If the values of ρ_s , μ_s , and $\lambda_{E,M}^s$ were known, it would be easy to optimize an experiment to find strange vector matrix elements. For example, if $|\rho_s| \sim 2$ and λ_E^s is small or negative, G_E^s would make a large contribution at $Q^2 > 0.5$ (GeV/c)² and small scattering angles. If λ_E^s is large and positive, the effects of a nonzero ρ_s are best observed at lower values of Q^2 . If $|\rho_s| \ll 2$, the experimental challenge is greater. Even if $\mu_s \sim -0.3$, the effect is an order of magnitude smaller at forward angles. At backward angles, one must contend with uncertainties in the term in Eqn. 34 that contains the axial form factor as discussed in Section 3.3 below.

A few publications address the Q^2 dependence of the strange form factors, but the models do not agree. One has a significant negative λ_E^s , and another has a large positive λ_E^s . Therefore, experiments searching for a nonzero G_E^s must cover a large range of Q^2 .

3.2 Electromagnetic Form Factors

As apparent from Eqn. 34, all of the electromagnetic form factors (EMFF) of both the proton and neutron are required in order to isolate the strange form factors. In this section we will discuss the present knowledge of the EMFF's.

3.2.1 Proton Form Factors

The traditional method for determining the EMFF's is to measure the elastic cross section given by

$$\frac{d\sigma}{d\Omega} = \frac{d\sigma}{d\Omega}\bigg|_{Mott} \left\{ \frac{G_E^2 + \tau G_M^2}{1 + \tau} + 2\tau G_M^2 \tan^2(\theta/2) \right\} \left\{ 1 + \frac{2E}{M} \sin^2(\theta/2) \right\}.$$

Data obtained at the same Q^2 but different angles may be combined to extract both the electric and magnetic form factors. This procedure is known as the Rosenbluth separation.

Most information prior to 1990 was obtained from the Rosenbluth separation. To first order, the form factors are described by the “dipole” fit with the “Galster parameterization” for G_E^n [38]:

$$G_E^p = G_D \equiv (1 + \lambda_D \tau)^{-2}; \quad G_M^p = \mu_p G_D \quad (40)$$

$$G_E^n = -\mu_n \tau G_D (1 + \lambda_n \tau)^{-1}; \quad G_M^n = \mu_n G_D,$$

where the magnetic moments of the proton(neutron) are $\mu_p = 2.79(\mu_n = -1.91)$, $\lambda_D = 4.97$ and $\lambda_n = 5.6$.

The Rosenbluth separation method works best when $G_E^2 \sim \tau G_M^2$, which is the case for the proton near $Q^2 \sim 0.5(\text{GeV}/c)^2$. This condition is not met for the proton at large Q^2 values or for the neutron where $G_E^n \ll G_M^n$. For these cases, the angular dependence of the cross section is small and hard to isolate from systematic experimental errors or small theoretical corrections.

Much greater sensitivity from small contributions due to small EMFF's can be achieved by using spin-dependence in elastic scattering. This method was suggested by Akhiezer and Rekalov [39] in 1974. The first spin-dependent elastic scattering measurement was published in 1976 [40], but had limited precision. However, with recent developments in polarized electron beams, polarized targets, and recoil polarimeters, spin-dependence has become the method of choice.

One recent example is an experiment at the Thomas Jefferson National Accelerator Facility (JLab) that measured the polarization of the recoil proton scattered by polarized electrons [41]. The relevant formula is

$$\frac{G_E}{G_M} = -\frac{P_t}{P_l} \frac{(E + E')}{2M} \tan^2(\theta/2). \quad (41)$$

where $P_{t(l)}$ is the transverse(longitudinal) polarization of the recoil proton. The longitudinal polarization of the recoil proton precesses in the spectrometer magnet and contributes to a vertical polarization component. The above formula has two important features that yield excellent precision:

- The measured quantities are *linear* in G_E . Therefore, there is no amplification of errors due to subtractions of almost equal numbers.
- Only ratios of measured quantities are needed. The beam polarization and polarimeter analyzing power cancel.

Instead, the systematic errors arise from any lack of azimuthal symmetry in the polarimeter and any errors in understanding the precession of the proton spin in the recoil spectrometer magnet.

A summary of selected points from global analyses of cross section data [42, 43] together with the spin-dependence data mentioned above is shown in Figure 1. The cross section data are consistent with the hypothesis that $\mu G_E^p = G_M^p$ over the Q^2 range shown. However, the form factor data derived from the spin-dependent measurements are inconsistent with this hypothesis, and the discrepancy increases with increasing Q^2 .

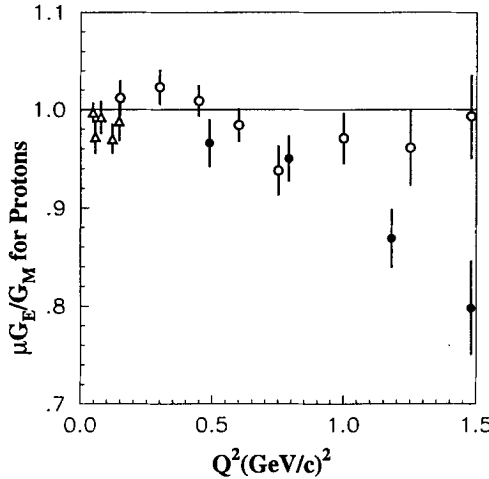


Figure 1: Data on $\mu G_E^p/G_M^p$. Open circles [42] and triangles [43] are from global analyses of cross section data. Closed circles are from the recent recoil polarimeter experiment. [41]

The asymmetry A_{PV} depends on ratios of form factors. Often form factors are measured relative to G_D , so the ratio $G_M^p/(\mu_p G_D)$ is required. Results from global analyses [42, 43] for G_M^p are shown in Figure 2. There is general agreement that the ratio $G_M^p/(\mu_p G_D)$ approaches 1.04 as Q^2 rises to 1.5 (GeV/c)². For the region near $Q^2 = 0.3$, the different analyses draw quite different conclusions. In this region, $G_M^p/(\mu_p G_D)$ may be near unity or it may be as low as 0.95.

3.2.2 Neutron Form Factors

Much of the contribution to A^{PV} comes from a term proportional to G_M^n . Hence precision determination of G_M^n is required over a range of Q^2 in order to extract the strangeness contribution without additional errors. However, G_M^n measurements are difficult since there are no free neutron targets. One accepted method is the comparison of the reactions $D(ee'n)$ and $D(ee'p)$ [44, 45, 46]. Another method is to use spin dependence in the $^3\text{He}(\bar{e}e')$ reaction. Recent data [47, 48] are shown in Figure 3. For the experiments that measure a ratio of cross sections [44, 45, 46], it is important to have knowledge of the value assumed by the authors for $G_M^p/\mu_p G_D$. This is especially important given the variations found in the literature, as mentioned above. The data are inconsistent by 10% or more. This difference will change the strange form factors much more than the projected errors of future experiments. Hence it is important that the experimental situation be improved.

By far the biggest concern in extracting strange matrix elements has been the experimental knowledge of G_E^n . The “Galster approximation” was believed to be reliable to 50% at best. Data on elastic scattering from deuterium [49] gave similar limits. Recently, extensive data on spin-dependent scattering has been obtained [50, 51, 52, 53, 54]. The data are consistent with the shape assumed in the Galster parameterization but seem to be about 10% larger. Errors on the order of $\pm 20\%$ are now appropriate.

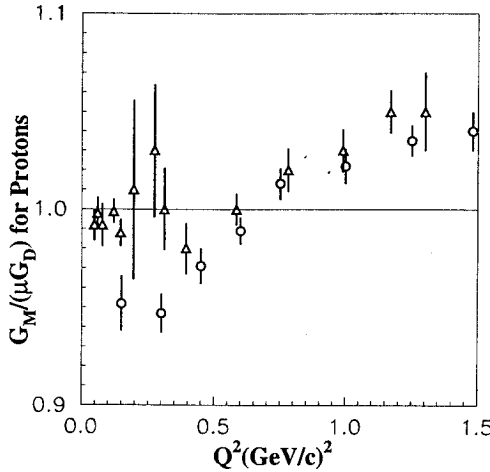


Figure 2: Data on $G_M^p/(\mu_p G_D)$. Open circles [42] and triangles [43] are from global analyses of cross section data.

3.3 Radiative Corrections

The advantage of the Standard Model of electroweak interactions is that it is renormalizable. In principle, higher order corrections can be computed reliably. Moreover, given that the coupling constant $\alpha_\gamma/4\pi \sim 0.001$, the corrections should be small. Thus, one would expect the tree level result of Eqn. 34 to be sufficiently accurate.

Unfortunately this picture is naive, especially for the axial proton current. Factors like $\ln(M_Z^2/M_p^2)$ increase the size of the corrections. For tree level terms proportional to $1 - 4\sin^2\theta_W \sim 0.08$, the *relative* size of the radiative corrections is further enhanced. For the axial-vector coupling, the radiative correction is of the order [61]

$$\frac{1}{1 - 4\sin^2\theta_W} \frac{\alpha}{4\pi} \ln \frac{M_Z^2}{M_p^2} \sim 0.1. \quad (42)$$

In addition, radiative corrections involve hadronic structure that is difficult to compute reliably.

The full expression for A_p^{PV} is

$$A^{PV} = \left[\frac{-G_F M_p^2 \tau}{\pi \alpha \sqrt{2}} \right] \left\{ \hat{\rho}'_{eq} (1 - 4\hat{\kappa}'_{eq} \hat{s}_Z^2) - \frac{\hat{\rho}'_{eq} [\varepsilon G_E^{p\gamma} (G_E^{n\gamma} + G_E^s) + \tau G_M^{p\gamma} (G_M^{n\gamma} + G_M^s)]}{\varepsilon (G_E^{p\gamma})^2 + \tau (G_M^{p\gamma})^2} - \frac{\sqrt{\tau(1+\tau)} \sqrt{1-\varepsilon^2} G_M^{p\gamma} \Lambda_Z}{\varepsilon (G_E^{p\gamma})^2 + \tau (G_M^{p\gamma})^2} \right\}, \quad (43)$$

where $\hat{\rho}'_{eq}$, $\hat{\kappa}'_{eq}$, \hat{s}_Z^2 , and Λ_Z are quantities defined below. The \overline{MS} renormalization scheme is used.

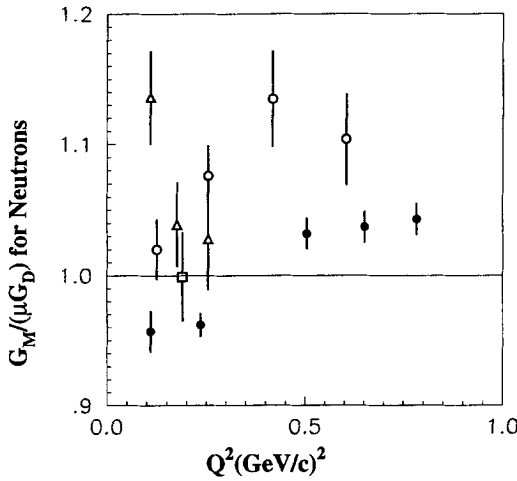


Figure 3: Data on $G_M^n/(\mu_n G_D)$: solid circles [44, 45], open circles [46], triangles [47], and square [48].

The radiative corrections for the terms involving the vector form factors are small and well known [62]. One reason is that the radiative corrections have a $1 - \sin^2 \theta_W$ suppression relative to the largest tree-level terms, opposite to the case for the axial corrections. In particular, the asymmetry is multiplied by a factor near unity, $\hat{\rho}'_{eq} = 0.9897$ [20]. The value for \hat{s}_Z^2 has a small correction factor $\hat{\kappa}'_{eq} = 1.0029$. These corrections are small compared to projected errors in the experiments. Uncertainties due to hadronic effects are also small.

The third term in the expression, due to the axial hadronic current, includes the constant Λ_Z . It is discussed in detail in the following section.

3.3.1 The Axial Proton Current

The radiative corrections to the axial proton current in electron scattering are substantial. Moreover, all of the diagrams have not been calculated. The radiative corrections may be included in the coefficient Λ_Z for the phenomenological four-fermion interaction defined as follows:

$$L^{int} \equiv \frac{G_F}{\sqrt{2}} \Lambda_Z \bar{e} \gamma^\mu e \bar{u}_p \gamma_\mu \gamma_5 u_p. \quad (44)$$

At the tree level

$$\Lambda_Z^{tree} = (1 - 4 \sin^2 \theta_W) \left(-G_A^{(1)} + \frac{1}{2} F_A^s \right). \quad (45)$$

Here we use superscripts to denote various approximations to Λ_Z

The radiative corrections have been computed for the “single quark” diagrams such as the one illustrated in Figure 5 a) and are given in Ref. [20]. The results are quoted in terms of phenomenological

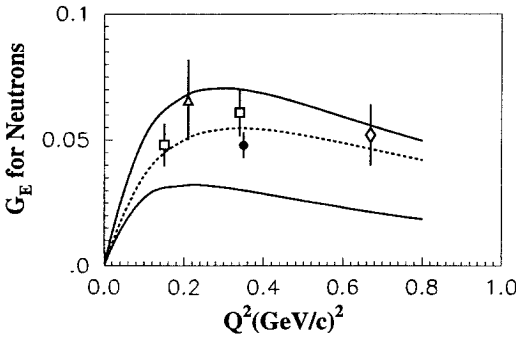


Figure 4: Recent data on G_E^N . Dotted line is the “Galster approximation.” Solid lines are limits allowed by data from Saclay. [49]. Squares are from Mainz [50, 51], triangle from NIKHEF [52], diamond from Mainz [53], and circle from Mainz. [54]

Table 3: Axial quark currents of the proton based on various assumptions from Ref. [14].

Current	$SU(3)_f$	Symmetric	Antisymmetric
Δu	0.82	0.83	0.81
Δd	-0.44	-0.43	-0.45
Δs	-0.11	-0.16	-0.08

couplings C_{2i} defined by

$$L^{int} \equiv \frac{G_F}{\sqrt{2}} C_{2i} \bar{e} \gamma^\mu e \bar{u}_i \gamma_\mu \gamma_5 u_i, \tag{46}$$

where i denotes the quark flavor. In this approximation, we have

$$\Lambda_Z^{1-quark} \equiv (C_{2u} F_A^u + C_{2d} F_A^d + C_{2s} F_A^s). \tag{47}$$

Updated values of C_{2i} are given in Ref. [20]. At tree level,

$$C_{2u} = -C_{2d} = -C_{2s} = -\frac{1}{2} + 2 \sin^2 \theta_W. \tag{48}$$

In this approximation, Eqn. 45 is obtained.

When the “single” quark radiative corrections are included [55, 56, 57, 58, 59, 62] in the \overline{MS} scheme the values are [20]:

$$C_{2u} = \rho_{eq} \left(-\frac{1}{2} + 2\hat{\kappa} \hat{s}_Z^2 \right) + \lambda_{2u} = -.0359 \tag{49}$$

$$C_{2d} = \rho_{eq} \left(+\frac{1}{2} - 2\hat{\kappa} \hat{s}_Z^2 \right) + \lambda_{2d} = .0263. \tag{50}$$

Here $\rho_{eq} = 1.0009$, $\hat{\kappa}_{eq} = 1.0304$, and $\lambda_{2d} = 0.0026$, $\lambda_{2u} = -0.0121$, and $\hat{s}_Z^2 = 0.23124 \pm 0.00017$. A feature of including the radiative corrections is that all of the F_A^i are now required.

We can relate the F_A^i to the Δq_i from DIS spin structure studies:

$$F_A^u(0) = 2\Delta u \quad F_A^d(0) = 2\Delta d \quad F_A^s(0) = 2\Delta s \quad (51)$$

$$F_A^u(0) - F_A^d(0)/2 = G_A^{(1)} = (\Delta u - \Delta d) = g_A = 1.267 \quad (52)$$

$$[F_A^u(0) + F_A^d(0)]/2 = \Delta u + \Delta d = 0.4 \quad (53)$$

$$F_A^s(0)/2 = \Delta s = -0.1. \quad (54)$$

The values of the Δq_i s are given in Table 3. The Q^2 dependence of the isovector axial form factor is given in Eqn. 33. We will assume that the other form factors have similar Q^2 dependence. Given the small contribution of these form factors, this is a reasonable approximation. Thus, with the one-quark radiative corrections, we have

$$\Lambda_Z^{1-quark} = (C_{2u} - C_{2d})G_A^{(1)} + [C_{2u} + C_{2d}](\Delta u + \Delta d)G_A^D + 2C_{2d}\Delta sG_A^D, \quad (55)$$

where we have assumed that the Q^2 dependence of all of the axial form factors is the same and given by Eqn. 33.

The $\hat{\kappa}'_{eq}$ factor makes a 3% correction to $\sin^2 \theta_W$, and this in turn changes $1 - 4\sin^2 \theta_W$ by about 40%. The net effect of all the one-quark corrections to Λ_Z is 20% in the \overline{MS} scheme.

We comment briefly on the uncertainties in Δu , Δd , and Δs . Values from a recent paper by Lipkin and Karliner [14] are given in Table 3. The column labeled $SU(3)_f$ gives the most conventional analysis where $\Delta u - \Delta d - 2\Delta s = 3F - D = 0.71$ for $F/D = 0.64$ from hyperon decays and $F + D = g_A$. The effect of using different assumptions changes the contribution of Λ_Z by only about 5%.

3.3.2 Anapole Contributions

Additional radiative corrections are computed on the basis of an effective field theory using mesons [63, 64, 65, 66, 67]. The authors often denote these contributions (a parity-violating coupling of the photon to the proton) as the anapole moment. A typical Feynman diagram for an anapole contribution is shown in Figure 5 b). For elastic scattering, the anapole moment appears as a correction to the G_A term. The distinction between Figs. 5 a) and b) is not rigorous, and there may be some double counting, missing contributions, and trouble with gauge invariance.

Care must be taken to get all of the normalizations correct. A simple way that is essential to the method of Ref. [19, 67] is to normalize to the tree level axial isovector term in the *on shell* scheme:

$$\delta\Lambda_Z^{anapole} = (1 - 4\sin^2 \theta_W)(-1)(R_a^{T=1} + R_a^{T=0})G_A^{(1)}, \quad (56)$$

where the normalized R_a is defined to be the anapole contribution.

It is important to notice that Refs. [67] uses the on-shell renormalization scheme and the notation

$$\Lambda_Z = (1 - 4\sin^2 \theta_W)(-[1 + R_A^{T=1} + R_A^{T=0}]G_A^{(1)} + F_A^s/2), \quad (57)$$

where $\sin^2 \theta_W = 0.2230$ [On-Shell Scheme] [20]. Here, the R_A terms include both single quark terms and as well as the anapole contributions. Explicitly, $R_A^{T=1} = -0.35(-0.41 \pm 0.24)$, and $R_A^{T=0} = 0.06(0.06 \pm 0.14)$, where the first number is the “single quark” terms, and the second number includes the anapole moment R_a .

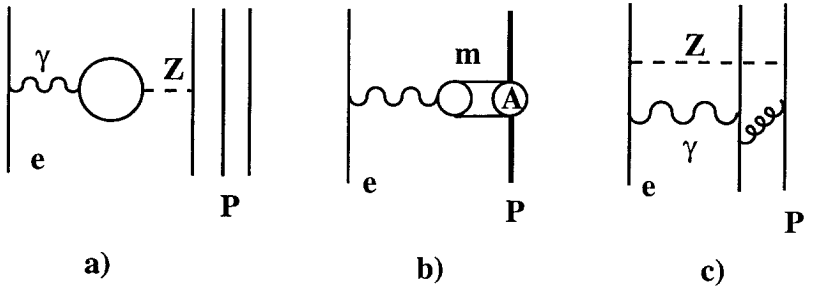


Figure 5: Feynman graphs representing radiative corrections. Included are a) single quark effects, b) anapole effects, and c) multi-quark box diagrams.

The interpretation and application of the corrections can be clouded by the large differences in the nominally equal quantities such as $1 - 4 \sin^2 \theta_W$, especially since this factor does not appear explicitly in the notation of Refs. [19] and [67]. Hence extreme care must be taken. One example is the coefficient of F_A^s . For Refs. [19] and [67], it is 0.11 whereas in the \overline{MS} formula it is 0.05. To include the anapole moment in the \overline{MS} formula, we have

$$\Lambda_Z = \left\{ (C_{2u} - C_{2d}) \left(1 + \frac{(1 - 4 \sin^2 \theta_W)}{C_{2u} - C_{2d}} [R_a^{T=1} + R_a^{T=0}] \right) G_A^{(1)} + \right. \quad (58)$$

$$\left. (C_{2u} + C_{2d})(\Delta u + \Delta d) G_A^D + C_{2d} F_A^s \right\} = -(0.080 \pm 0.033) G_A^D,$$

where $\sin^2 \theta_W = .2230$ and

$$\frac{(1 - 4 \sin^2 \theta_W)}{C_{2u} - C_{2d}} R_a^{T=1} = -0.10 \pm 0.41; \quad \frac{(1 - 4 \sin^2 \theta_W)}{C_{2u} - C_{2d}} R_a^{T=0} = -0.01 \pm 0.24. \quad (59)$$

The C_{2u} and C_{2d} are evaluated using $s_Z^2 = 0.23124$.

With the approach described above, the anapole moment uncertainty makes a substantial fractional contribution to the axial term. The hybrid notation used in the discussion is a bit clumsy, but it has the advantage that updated results of Ref. [20] can be used for the single quark terms, and the relatively simple normalization of Ref. [67] can be used for the anapole moment. Implicitly, we have assumed that all Q^2 dependence follows from the axial dipole form factor $G_A^D(Q^2)$. A recent paper by C. M. Maekawa and V. van Kolck suggests that this is a reasonable approximation for the anapole moment [66], further suggesting that the best mass is $M_A = 880$ MeV.

There are additional uncalculated multi-quark contributions such as the graph in Figure 5 c). Since they involve excited states of the nucleon, they are especially hard to estimate. Although no rigorous bound is available, we naively expect these corrections to be smaller than the quoted error on the anapole moment.

In conclusion, the axial radiative corrections are summarized by replacing the tree level expression

$$\Lambda_Z^{tree} = (1 - 4 \sin^2 \theta_W)(-G_A + F_A^s/2)$$

by

$$\Lambda_Z = -(0.080 \pm 0.033) G_A^D; \quad G_A^D = (1 + 3.32\tau)^{-2}. \quad (60)$$

The SAMPLE collaboration [78] uses the notation

$$G_A^Z = \Lambda_Z / (1 - 4 \sin^2 \theta_W), \quad (61)$$

where G_A^Z is a new hadronic axial form factor that includes the radiative corrections for parity-violating electron scattering. This notation emphasizes the hadronic aspect of the radiative corrections. With this definition, one must be especially careful as to which of the various possible values for $\sin^2 \theta_W$ is used.

Since $R_A^{T=1}$ is isovector, it can be measured by quasi-elastic scattering from deuterium. In this case, the asymmetry measured is given by Eqn. 36. This has been done recently by the SAMPLE collaboration as described below. The term $R_A^{T=0}$ is an isoscalar radiative correction that adds to the F_A^s term in electron scattering. By performing elastic neutrino scattering from the nucleon, [68] the effects of $R_A^{T=0}$ and F_A^s could be determined separately.

The above analysis assumes that the Standard Model gives a sufficiently complete description of the relevant interactions. Extensions to the Standard Model, such as extra Z bosons, would change these results.

3.4 Charge Symmetry Violations

A key assumption in the derivation of the equations that allow the extraction of strange form factors from data is charge symmetry. For protons the assumption is given in Eqn. 27 and for isoscalar nuclei in Eqn. 17.

For the nucleon, differences in the up and down quark masses as well as other possible mechanisms that violate charge symmetry contribute an extra term $G_{E,M}^{u,d}$ to Eqn. 31 as follows:

$$G_{E,M}^{pZ} = \frac{1}{4}(G_{E,M}^{p\gamma} - G_{E,M}^{n\gamma}) - \sin^2 \theta_W G_{E,M}^{p\gamma} - \frac{1}{4}G_{E,M}^s - \frac{1}{4}G_{E,M}^{u,d}. \quad (62)$$

Moreover, $G_{E,M}^{u,d}$ may be different for the neutron. The value of $G_{E,M}^{u,d}$ has been estimated by quark models [69, 70], a baryon-meson model [30], and by chiral perturbation theory [71]. The largest predicted effect by Ma is 0.088 [30], which is quite large. Lewis and Mobed [71] predict $G_M^{u,d} = 0.028 \pm 0.006$, and the other predictions are smaller. Miller [70] argues that the estimate of Ma represents a worst case and the effect is probably smaller. Thus, at present, it appears that uncertainties in the form factor measurements are much more important than possible violations of charge symmetry.

Additional isospin violating terms are present for nuclear targets [72, 73]. For example, the coulomb interaction changes slightly the density of protons relative to neutrons. Similar corrections are important for precise studies of Fermi beta decay. The contribution varies dramatically with Q^2 . Ormand estimates that his calculated corrections are reliable to $\pm 20\%$ of themselves. For ${}^4\text{He}$, the correction is $< 1\%$ except near the diffraction minimum. On the other hand, for ${}^{28}\text{Si}$, the correction is typically larger than 1% for $Q > 0.5\text{fm}^{-1}$.

Finally, we note that meson exchange currents can contribute to strange form factors for nuclei at large Q^2 [18]. Probably the best nucleus for studying such effects is ${}^4\text{He}$.

4 Experimental Technique

More than ten experiments using polarized electrons to study parity violation have either been completed [75, 76, 77, 78, 79] or are in progress [81, 82, 83, 85, 87]. A list is given in Table 4. These experiments share many of the same technical problems and use many of the same solutions. In this chapter, we discuss many of the common features.

Table 4: Survey of parity experiments using polarized electrons.

Experiment	Reaction	Physics	A^{PV}
Published Experiments			
SLAC E122 [75]	$\bar{e}D$ (DIS)	PV of Z	10^{-4}
Mainz [76]	$\bar{e}^9\text{Be}$ QE	New Physics	10^{-5}
Bates [77]	$\bar{e}^{12}\text{C}$ Elastic	New Physics	10^{-6}
SAMPLE(Bates) [78]	$\bar{e}P$ Elastic	$G_M^s(0) = \mu_s$	10^{-5}
HAPPEX(JLab) [79]	$\bar{e}P$ Elastic	$G_M^s + 0.39G_E^s$	10^{-5}
Approved Experiments			
Mainz [81]	$\bar{e}P$ Elastic	G_M^s, G_E^s	10^{-5}
G^0 (JLab) [82]	$\bar{e}P$ Elastic	G_M^s, G_E^s	10^{-5}
^4He (JLab) [83, 84]	$\bar{e}^4\text{He}$ Elastic	G_E^s	10^{-5}
Moller(SLAC) [85]	$\bar{e}e$	New Physics	10^{-7}
HAPPEX II(JLab) [86]	$\bar{e}P$ Elastic	$G_M^s + 0.39G_E^s$	10^{-6}
(JLab) [87]	\bar{e} Pb	Neutron Radius	10^{-6}
Possible new experiments			
(JLab)	$\bar{e}P$	New Physics	10^{-7}

4.1 Overview

In parity violating electron scattering experiments, one measures the helicity dependent left-right asymmetry in the scattering of longitudinally polarized relativistic electrons from unpolarized nuclear targets. The resulting asymmetries are small, requiring measurements with statistical and systematic errors substantially less than 1 part per million (ppm). This requirement leads to two overriding themes in the experimental technique. First, the physical properties of the incident beam on target and the experimental environment as a whole must be identical for the left- and right-handed beams to a very high degree so as to minimize spurious asymmetries. Second, innovative flux counting techniques must be used in order to accumulate sufficient statistics.

Indeed, all successful experiments to date have used a GaAs photocathode to produce polarized electrons, with the ability to rapidly and randomly flip the sign of the electron beam polarization. The asymmetry is extracted by generating the incident electron beam as a pseudorandom time sequence of helicity “windows” and then measuring the fractional difference in the integrated scattered flux over window pairs of opposite helicity. Due to the high rates, the integrated scattered flux is typically obtained by flux counting, where the response of a charged particle detector that intercepts the scattered electrons is integrated over the duration of each helicity window.

The flux counting technique implies that spectrometers must be chosen that guide the scattered electrons of interest into a region that is otherwise free of background, and detectors must be chosen whose response is dominated by the scattered electrons. Further, the electronics that record the detector signals must have sufficient resolution and be insensitive to electronic pickup. Finally, it is important that random fluctuations from sources such as beam jitter, target density fluctuations and electronics noise are minimized.

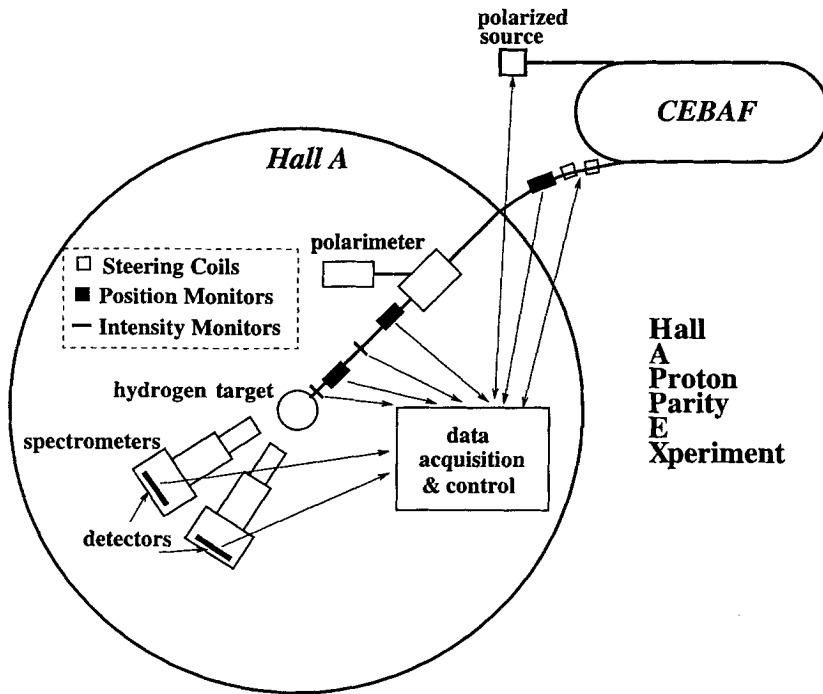


Figure 6: Schematic overview of the HAPPEX experiment at Jefferson Laboratory. Similar components are used for most parity-violation experiments with polarized electrons.

Apart from random jitter, an important class of potential false asymmetries arise from helicity-correlated fluctuations in the physical properties of the beam, such as intensity, energy and trajectory. These properties are therefore monitored with high precision. The sensitivity of the scattered flux to fluctuations in the beam parameters are evaluated continuously and accurately.

To extract the physics asymmetry from the measured experimental raw asymmetry, one needs to measure the longitudinal polarization of the incident electron beam accurately. Electron beam polarimetry has matured over the past two decades. There are two main techniques: Compton polarimetry and Møller polarimetry each of which have advantages and disadvantages.

Figure 6 shows a schematic diagram of the important components of the HAPPEX experiment, as a specific example of the important components of a parity violation experiment. In the following sections, we elaborate on the above considerations in detail, frequently commenting on choices made by specific experiments.

4.2 Polarized Electron Source

The production of polarized electrons whose characteristics remained virtually unchanged with reversal of helicity was a major early thrust of experimental design. After initial exploration of techniques

Table 5: Operating characteristics of polarized sources at major electron scattering facilities.

Facility	SLAC	Mainz	Bates	Jlab
Rep. Rate (Hz)	120	CW	600	CW
Peak Current (mA)	200	-	5	-
Average Current (μ A)	10	35	40	100
Beam Energy (GeV)	48	1.0	1.0	6.0
Beam Polarization	75	70	40	75

involving atomic sources [88], the breakthrough that made parity violating electron scattering experiments of high accuracy feasible was the development of the electron source based on photoemission from a Gallium Arsenide (GaAs) photocathode [89].

The electrons are produced by illuminating a GaAs photocathode with circularly polarized laser light (chemically treated to create a negative work function at the surface) that is placed at a positive potential (typically ~ 100 kV). The GaAs wafer is cleaved along a crystal axis such that the valence band is predominantly in a $p_{3/2}$ state and the conduction band is in an $s_{1/2}$ state. Further, the degeneracy of the sublevels of the valence band is broken by appropriate doping of the crystal [90]. The net result is that one or the other of the s -state sublevels of the conduction band is preferentially populated depending on the handedness of the incident circularly polarized light. The experimental realization of this concept made parity violation experiments feasible since:

- The sign of the polarization state can be changed rapidly, minimizing the impact of slow drifts.
- The characteristics of the laser light (which define the properties of the electron beam) can be accurately controlled by a variety of sophisticated feedback techniques.
- Electron sources of high average and instantaneous currents have been developed, enabling experiments of high luminosity.

The development of polarized sources for use in parity violation experiments was pioneered at SLAC [75, 90]. Since the first prototype, enormous strides have been made in improving the performance of the sources at SLAC as well as at Mainz, MIT-Bates and Jefferson Laboratory. Currently, beam polarization on target between 70% and 80% at high luminosity have been achieved at several laboratories. We list the main characteristics of the polarized sources at these major electron scattering facilities in Table 5.

4.3 The Raw Asymmetry Measurement

With the use of optical pumping at the polarized source, it is possible to produce time “windows” of longitudinally polarized electrons by appropriate modulation of the laser beam. With repetition rates typically between $\sim 10 - 1000$ Hz, each time window contains an electron ensemble of net positive or negative polarization, which we denote as positive or negative helicity events. Typically a pseudo-random helicity sequence is used in order to reduce any sensitivity to periodic noise in the accelerator environment.

Events of opposite helicity that are at the same phase with respect to the dominant 60 (or 50) Hz background noise in the accelerator electrical environment are chosen to form “window pairs”. The

scattered flux F is measured independently for every event, and thus one can obtain the cross section asymmetry A_i for the i th window pair. The raw asymmetry is then obtained by appropriate averaging of N measurements. If the experiment is designed carefully, the standard deviation $\sigma(A_i)$ is dominated by the counting statistics in the scattered flux, greatly minimizing potential problems in the averaging procedure:

$$A_i \equiv \left(\frac{F_R - F_L}{F_R + F_L} \right)_i; \quad A_{\text{raw}} = \langle A_i \rangle; \quad \delta(A_{\text{raw}}) = \sigma(A_i)/\sqrt{N}. \quad (63)$$

Indeed, all electronic signals in the experiments are designed so that electronic noise is small compared to $\sigma(A_i)$. Experiments that are currently under construction are being designed for $\sigma(A_i)$ less than 10^{-4} . The value of $\sigma(A_i)$ sets the scale for the noise requirements on the performance of the electron beam parameters and the associated instrumentation.

The two key parameters for each experimentally measured quantity M (such as detector rate, beam intensity etc.) is $\sigma(M)$ (the relative window-to-window fluctuations in M) and $\delta(M)$, the relative accuracy with which M can be measured compared to the true value of the fluctuating input. If $\sigma(M)$ is large enough, it might mean that there are non-statistical contributions to $\sigma(A_i)$ so that the latter is no longer dominated by counting statistics. In this case, it is crucial that $\delta(M) \ll \sigma(M)$ so that window to window corrections for the fluctuations in M can be made to A_i . We discuss this issue in the next section.

An important benchmark for the experimental measurement is to plot A_i for the entire data sample. If all sources of noise are properly handled, this distribution should be a perfect Gaussian over many orders of magnitude, reflecting the counting statistics of the scattered electron flux. Figure 7 shows the raw window asymmetry for 30 Hz window pairs during the first phase of the HAPPEX experiment.

4.4 Beam Fluctuations

The detector output is integrated over the duration of each helicity window and digitized, thus providing a number D proportional to the total number of scattered electrons incident on the detector during each window. One obtains the normalized flux F for a helicity window by dividing D by the integrated, digitized charge I over the same window. We rewrite Eqn. 63 here for convenience:

$$A_i = \left(\frac{F_R - F_L}{F_R + F_L} \right)_i \simeq \left(\frac{\Delta F}{2F} \right)_i, \quad (64)$$

where $\Delta X \equiv X_R - X_L$.

4.4.1 Random Fluctuations

As discussed above, one would like $\sigma(A_i)$ to be dominated by counting statistics. However, fluctuations $\sigma(X_i)$ in the beam parameters X_i can contribute significantly to $\sigma(A_i)$. For example, typical window-to-window relative beam intensity fluctuations ($\sigma(\Delta I/2I)$) on target at pulsed accelerator facilities is about 1%. The detector-intensity correlation can be exploited to remove the dependence of beam charge fluctuations on the measured asymmetry:

$$A_i \simeq \left(\frac{\Delta F}{2F} \right)_i \simeq \left(\frac{\Delta D}{2D} - \frac{\Delta I}{2I} \right)_i. \quad (65)$$

For experiments that have been published to date, only intensity fluctuations were substantial enough to significantly affect $\sigma(A_i)$. However, for the next generation of experiments, $\sigma(A_i)$ will be one to two

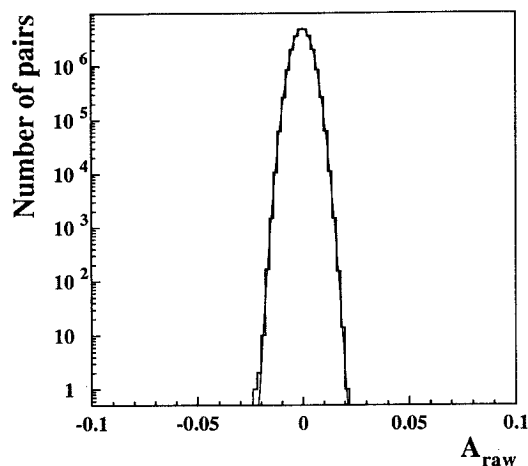


Figure 7: Raw Window Pair Asymmetry for the first phase of the HAPPEX experiment, where $\sigma(A_i)$ was 3.8×10^{-3} .

orders of magnitude smaller. At this level, residual contributions from random fluctuations in energy, position and angle are likely to be significant. In order to measure the asymmetry to the limit of the true counting statistics, it is therefore important to make corrections for random window-to-window fluctuations of the average intensity, position and angle.

The corrections can be parameterized as follows:

$$A_i = \left(\frac{\Delta D}{2D} - \frac{\Delta I}{2I} \right)_i - \sum_j \left(\alpha_j (\Delta X_j)_i \right). \quad (66)$$

Here, X_j are beam parameters such as energy, position and angle and $\alpha_j \equiv \partial F / \partial X_j$ are coefficients that depend on the kinematics of the specific reaction being studied as well as the detailed spectrometer and detector geometry of the given experiment.

By judicious choices of beam position monitoring devices (BPMs) and their respective locations, several measurements of beam position can be made from which the average relative energy, position and angle of approach of each ensemble of electrons in a helicity window on target can be inferred. Alternatively, one can write

$$A_i = \left(\frac{\Delta D}{2D} - \frac{\Delta I}{2I} \right)_i - \sum_j \left(\beta_j (\Delta M_j)_i \right). \quad (67)$$

Here M_i are a set of 5 BPMs that span the parameter space of energy, position and angle on target and $\beta_i \equiv \partial F / \partial M_i$.

It is worth noting that this approach of making corrections window by window automatically accounts for occasional random instabilities in the accelerator (such as klystron failures) that are characteristic of normal running conditions. An important consideration is the precision $\delta(M_i)$ with which one can make corrections window by window for the various beam parameters. A further consideration is the accuracy with which the coefficients β_i are measured. These errors determine whether $\sigma(A_i)$ is dominated by counting statistics.

4.4.2 Systematic Fluctuations

The considerations of the previous section should ensure that the measured $\sigma(A_i)$ has negligible contributions from window-to-window beam fluctuations and instrumentation noise. However, after averaging over many window pairs, it is quite plausible that a small helicity-correlated fluctuation in a beam parameter might give rise to a false asymmetry at the ppm level. If one considers the cumulative experimental asymmetry A_{exp} over many window pairs, one can write

$$\begin{aligned} A_{\text{exp}} \equiv \langle A_i \rangle &= \left\langle \left(\frac{\Delta D}{2D} \right)_i \right\rangle - \left\langle \left(\frac{\Delta I}{2I} \right)_i \right\rangle - \sum_j \beta_j \langle (\Delta M_j)_i \rangle \\ &= A_D - A_I - \sum_j A_{M_j}. \end{aligned} \quad (68)$$

Ideally, one would like $A_{\text{exp}} \simeq A_D$, which would mean that all corrections are negligible. Indeed, for the recently published HAPPEX result from Jefferson Laboratory, this was the case. However, for future experiments, a more realistic goal is to ensure that the systematic error is small compared to the statistical error $\delta(A_{\text{exp}})$ in the extracted experimental asymmetry A_{exp} .

For the case of A_I , it is sufficient to have $A_I \sim A_{\text{exp}}$. The detector and beam flux instrumentation can be designed to have a linearity better than 1%, which leads to a negligible systematic error when one makes a correction A_I , which is as big as (but not much bigger than) A_{exp} . For A_{M_j} , it is important that each term be of the order of the statistical error $\delta(A_{\text{exp}})$. This is because one might expect systematic errors of order 10% on the determinations of the coefficients β_j . If the A_{M_j} corrections are much bigger than the final statistical error, the result might have a substantial systematic error.

The control of the asymmetry corrections within the abovementioned constraints is one of the central challenges during the running of parity experiments. A variety of feedback techniques on the laser and electron beam properties are employed during data taking in order to accomplish this; these methods are discussed in Sec. 4.6. Another way to alleviate the size of the corrections is to have significant symmetry in the experimental apparatus, which would reduce the size of the coefficients β_j . For example, an azimuthal symmetry in the acceptance of scattered electrons greatly reduces the sensitivity of the average experimental cross-section to position fluctuations.

4.4.3 Beam Dithering

In order to measure the correlation coefficients β_j , a beam dithering technique has been employed in some published experiments at Bates and Jefferson Lab. During data taking, the beam parameters would be varied (at rates that are slow compared to the helicity flipping frequency) in a controlled way by perturbing corrector coils to vary position and angle as well as a radiofrequency module to vary the energy. We briefly discuss the formalism for how the coefficients $\beta_j \equiv \partial\sigma/\partial M_i$ are extracted from the dithering data.

First, the response of the scattered flux and the BPMs to corrector coils C_j are measured: $\partial F/\partial C_j$ and $\partial M_i/\partial C_j$. The β_i are then obtained by solving the matrix equation:

$$\frac{\partial F}{\partial C_j} = \sum_i \left(\frac{\partial F}{\partial M_i} \right) \left(\frac{\partial M_i}{\partial C_j} \right) = \sum_i \beta_i \left(\frac{\partial M_i}{\partial C_j} \right) \rightarrow \beta_i = \sum_j \left(\frac{\partial F}{\partial C_j} \right) \cdot \left(\frac{\partial M_i}{\partial C_j} \right)^{-1}. \quad (69)$$

The key to the success of the method is to ramp, under computer control, a complete set of parameters with devices placed upstream of all BPMs. There are important dynamic range criteria to be considered. Firstly, the coils must vary the position and angle with ample independence so that the matrix $\partial M_i/\partial C_j$ is far from being singular, since it must be inverted to obtain the coefficients. The amplitude of the ramping must be large enough to exceed the normal beam jitter but small enough so that the statistical error on the cross-section is not degraded. This method is crucial to be able to take production data and study systematic errors simultaneously.

To demonstrate how well these considerations work out in practice, we show data from the HAPPEX experiment in Figure 8. The top plot shows the helicity-correlated horizontal beam position asymmetry as measured by a BPM close to the target. The data have been spit into 20 data sets, each corresponding to roughly one full day of running at peak luminosity. The bottom two plots show the computed correction $\sum A_{Mj}$ for the left and right spectrometers. It can be seen that the corrections are of order 0.2 ppm ($A_{exp} \sim 10$ ppm) except for the last few data sets, where the corrections became as large as 1 ppm. The cumulative statistical error in the final result was $\delta(A_{exp}) = 0.75$ ppm. It is worth noting that there is a partial cancellation between the corrections in the right and left spectrometers.

4.5 Electron Beam Monitoring

The above discussion regarding measurement accuracy and its impact on $\sigma(A_i)$ is particularly relevant in the monitoring of the electron beam properties such as beam intensity, trajectory and energy. The performance for experiments that have taken data so far have been $\delta(X) \sim 10\mu\text{m}$, $\delta(\theta_x) \sim 1\mu\text{rad}$, $\delta(E)/2E \sim 10^{-4}$ and $\delta(I)/2I \sim 10^{-3}$, where X and θ_x are position and angle coordinates, E is the beam energy and I is the beam intensity.

The standard deviation $\sigma(M)$ for each beam parameter M has typically been comparable to or smaller than the corresponding accuracy $\delta(M)$ and neither parameter has been large enough to significantly impact $\sigma(A_i)$ in the experiments carried out to date. For the next generation of approved experiments, the beam fluctuations and measurement accuracy will no longer be small enough to be neglected towards a contribution to $\sigma(A_i)$. Future experiments will require $\delta(X) \sim 1\mu\text{m}$, $\delta(E)/2E \sim 10^{-5}$ and $\delta(I)/2I \sim 3 \times 10^{-5}$, better than an order of magnitude improvement over previous experiments. Improvements in instrumentation are now under way in order to satisfy these requirements.

At SLAC and MIT-Bates, the beam position monitors (BPMs) are assemblies of microwave cavities which are resonant at the microwave frequency of the accelerator cavities [91]. The rf electronics that processes the output of the BPMs has worked reliably for published experiments. However, for the next generation of experiments, improved processing electronics are needed. The anticipated performance is $1\mu\text{m}$ for each beam pulse which contains $\sim 5 \times 10^{11}$ electrons [92]. Figure 9 shows the result of a recent beam test of the new electronics at SLAC in preparations for experiment E158. Three BPMs were placed in a string in the 1 GeV section of the accelerator, and two of the BPMs were used to predict the position at the third BPM. The resulting residuals show a resolution better than $0.5\mu\text{m}$.

At Jefferson Lab, the cw nature of the beam precludes the use of the SLAC BPMs. Instead, the beam position is measured by “stripline” monitors, each of which consists of a set of four plates placed symmetrically around the beam pipe. The plates act as antennae that provide signals (modulated by the microwave structure of the electron beam) proportional to the beam position as well as intensity.

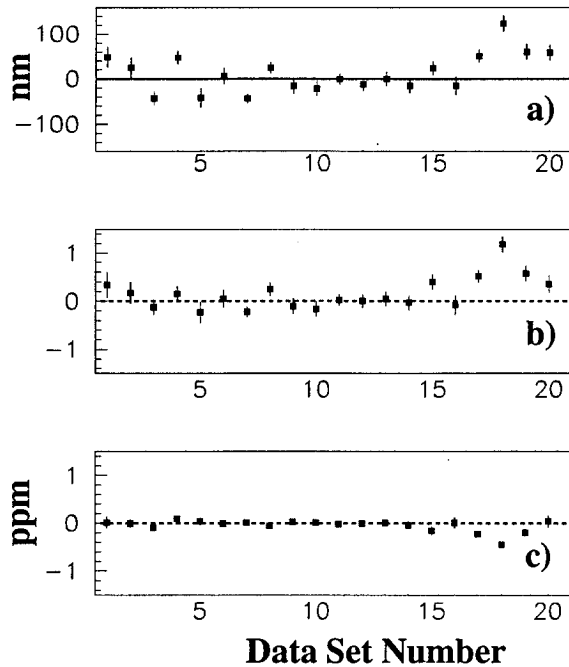


Figure 8: Asymmetry correction data from the HAPPEX experiment showing (a) Helicity correlation in a position monitor near the target, (b) and (c) Correction in both spectrometers due to the analysis including all helicity-correlated monitor differences.

The stripline BPMs are intrinsically noisier than cavity BPMs. However, good resolution is still possible at Jefferson Laboratory due to the high beam intensity. Figure 10 shows the correlation between the measured position at a BPM near the target compared with the predicted position using neighboring BPMs for a beam current of $100 \mu\text{A}$. A precision close to $1 \mu\text{m}$ was thus obtained for the average beam position for a beam window containing 2×10^{13} electrons. If the same level of precision is required at much lower beam currents, then microwave cavity monitors suitable for cw electron beams will have to be developed.

The beam intensity at SLAC and MIT-Bates is measured by current monitors, each of which consists of a toroidal ferrite core with enameled wire wrapped around it [93]. The signal produced by the wire can, in principle, provide a relative measurement of the beam flux with a precision better than 10^{-4} , which is required by the next generation of experiments. However, this has yet to be demonstrated and the development of appropriate processing electronics is underway for the E158 experiment at SLAC. The design goal is to achieve 3×10^{-5} relative precision for a beam charge of 3.5×10^{11} electrons and intensity jitter of 1%.

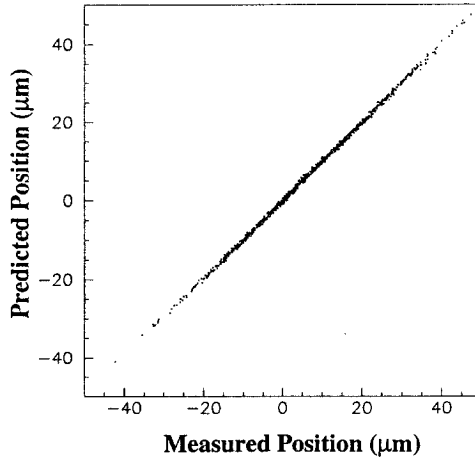


Figure 9: Window to window beam jitter as measured by a BPM of a 1 GeV electron beam at SLAC is plotted along the X-axis. On the Y-Axis is plotted the beam position as predicted by two other nearby BPMs. The residuals show a resolution better than $0.5 \mu\text{m}$.

At Jefferson Laboratory, microwave cavity BPMs have been developed for the measurement of beam intensity. The precision that has been achieved for a 30 ms beam window at $100 \mu\text{A}$ is 4×10^{-5} and is about 10^{-4} at $10 \mu\text{A}$. This is within a factor of two to three of what would be required for the next generation experiments.

The relative fluctuations in beam energy are obtained by measuring the average beam position with a monitor placed at a location of high dispersion in the accelerator. The design goals for the precision in beam position are usually sufficient in order to achieve the desired precision in the measurement of relative beam energy. However, for the next generation of experiments, the linearity over the full range of beam positions available for measurement in a given position monitor may become an issue, since the relative beam energy for a window must be measured to a precision of 10^{-5} .

4.6 Control of the Laser Light

The helicity windows are created by modulating the linearly polarized laser light before it is transported to the photocathode. The linearly polarized light is converted to circularly polarized light by means of a Pockels cell which is an electro-optic device whose birefringence is proportional to an applied electric field. The handedness of the circular polarization determines the sign of the longitudinal polarization of the electron beam.

Since the electromagnetic forces responsible for acceleration and beam transport are insensitive to electron helicity, virtually all systematic helicity-correlated differences in the physical properties of beam windows of opposite helicity can be traced back to systematic differences in the properties of the laser beam. An important thrust of experimental design is the ability to minimize these systematic differences by manipulating the properties of the laser beam.

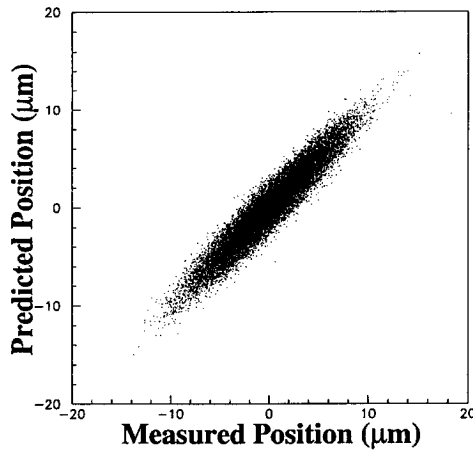


Figure 10: Window to window beam jitter as measured by a BPM of a 3 GeV electron beam at Jefferson Laboratory is plotted along the X-axis. On the Y-Axis is plotted the beam position as predicted by nearby BPMs. The residuals show a resolution better than 1 μm .

4.6.1 Dominant Effects: Intensity Asymmetry and Electronic Pickup

All experiments select the beam helicity for each window using a pseudorandom sequence. Depending on the repetition rate for helicity windows, complementary pairs of oppositely paired windows are judiciously chosen to be at the same phase with respect to the primary frequency of the power line. The helicity state for each beam window is usually prepared at the heart of the source electronics and the information is then delivered to the Pockels cell power supplies. The helicity state and Pockels cell supply circuitry are usually isolated electrically from the rest of the experiment. Great care must be taken in transmitting the helicity information to the experimental data stream in order to avoid generating spurious false asymmetries in the monitor and detector electronics. It is fairly easy to generate a crosstalk induced false asymmetry as large as 100 ppm, and the ultimate goal is to achieve a suppression of 4 orders of magnitude. Experiments employ a variety of electrical and timing isolation techniques in order to minimize these effects.

The dominant helicity correlated effect on the electron beam is an intensity modulation. In reality, the laser light exiting the Pockels cell is elliptically polarized. The laser transport system as well as the GaAs photocathode possess analyzing power that modulate the residual linear polarization of the laser beam. The result is that the electron beam intensity depends on helicity. The effect is schematically portrayed in Figure 11.

An intensity correlation at the electron source can induce an energy correlation, since the accelerator is slightly resistive. Further, since no accelerator is perfectly achromatic, these energy correlations can propagate into position and angle correlations in the electron beam on target. It is therefore important to reduce the intensity correlation to the ppm level at the polarized source over the duration of the experiment.

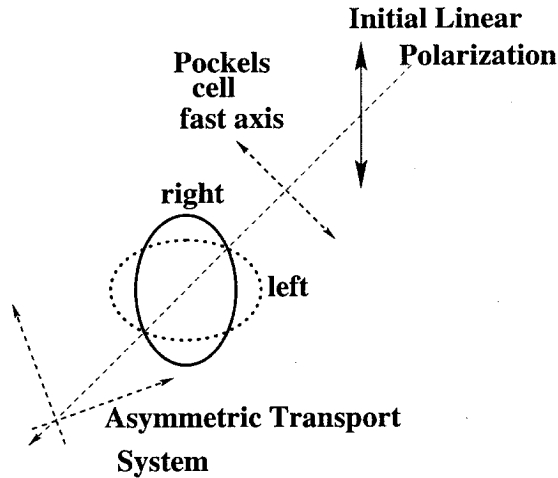


Figure 11: Schematic diagram showing how laser beam properties (and hence the electron beam properties) can depend on helicity.

All experiments employ a feedback loop to dynamically control the helicity correlation in beam intensity. One technique is to use the intrinsic dependence of the intensity asymmetry on the potential difference applied across the voltage of the Pockels cell that generates circularly polarized light. This technique was pioneered during the MIT-Bates ^{12}C experiment. More recent experiments use a dedicated Pockels cell sandwiched between two crossed polarizers to generate a helicity correlated intensity asymmetry that exactly cancels out the observed electron beam intensity asymmetry over a certain time period.

The original technique (making small changes on the primary Pockels cell) was also used during the HAPPEX experiment at Jefferson Laboratory. Figure 12 shows the variation of the helicity correlated intensity asymmetry in the electron beam as a function of the Pockels cell voltage. Figure 13 shows a schematic of the intensity feedback system. In addition, the schematic diagram also shows the approach taken at HAPPEX to reduce spurious electronic asymmetries by imposing all electrical communication with the polarized source electronics to be via fiber optic cables. Over the course of the experiment, the cumulative helicity correlated beam flux asymmetry was measured to be about 0.3 ppm.

4.6.2 Helicity Correlated Position Differences

Once the dominant intensity correlation is under control, the next important issue is helicity correlated position differences in the electron beam. The Pockels cell that converts linearly polarized light to left- or right- circularly polarized light can induce position differences in several ways. An intensive study of the physics of the mechanisms that give rise to such position differences is now under way at several laboratories. The effects are greatly enhanced for the case of the strained GaAs photocathode. For future experiments that plan to measure sub-ppm asymmetries with high polarization photocathodes, controlling these position fluctuations will be a very important issue.

One important effect is a helicity correlated angular deviation at the Pockels cell which results in the

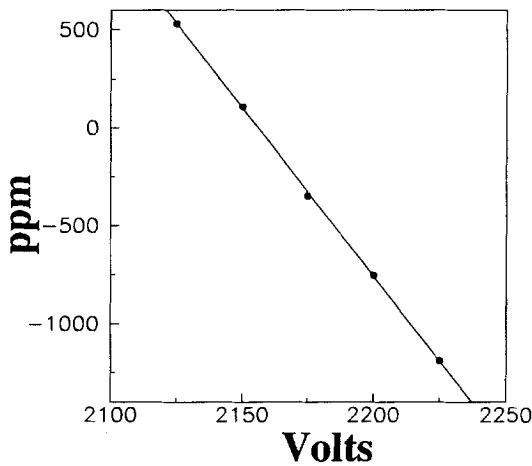


Figure 12: Intensity feedback at the HAPPEX experiment: the helicity-correlated electron beam intensity asymmetry is plotted as a function of the Pockels cell voltage. The curve is a straight line that crosses zero, a situation that is ideal for a dynamic feedback loop.

laser beam impinging at two different average centroids at the photocathode. This size of this effect is usually a few μ rad and the solution is to place a converging lens in the laser beam path that images the face of the Pockels cell on to the photocathode. The lens usually reduces the helicity correlated angular fluctuations by more than an order of magnitude.

The two newly published experiments SAMPLE and HAPPEX have observed further helicity correlated position fluctuations beyond simple angular deviations. At SAMPLE, measurements on the laser beam indicated that the beam centroid at the exit face of the Pockels cell was significantly different for the left- and right-handed circular polarizations. This effect was reduced by an order of magnitude by adding a feedback system involving a tilted plate on a piezoelectric mount in the laser beam [94]. A small helicity-correlated plate tilt angle was induced which effectively cancelled out the observed helicity-correlated difference in the laser beam centroid. This method greatly reduced the systematic position corrections that had to be made to the observed parity-violating asymmetry, as can be seen from Figure 14.

At HAPPEX, very significant helicity correlated position differences were observed in the electron beam when a high polarization strained photocathode was used. The HAPPEX experiment took an important new step in monitoring instrumentation by installing new BPMs after the very first acceleration section of the linac, where the electron beam energy was 5 MeV. The electron beam position fluctuations are greatly damped by the process of acceleration. It is therefore very important to measure position fluctuations as early as possible in the accelerator.

During a dedicated development run before the high polarization data taking phase of HAPPEX, helicity-correlated position shifts of several μ m were measured at the 5 MeV point. The solution that worked well for HAPPEX was to place a half-wave plate in the laser beam path just before the laser

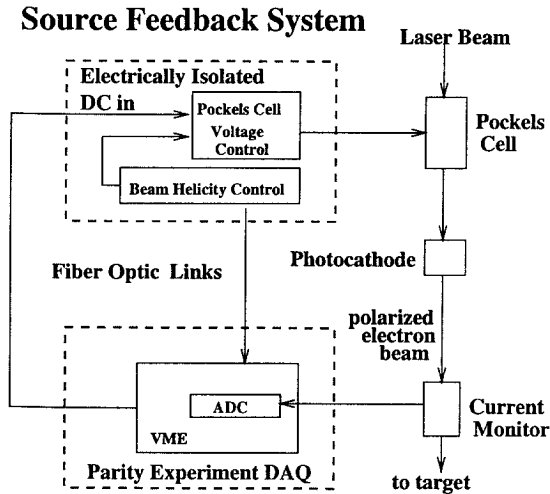


Figure 13: Schematic diagram of the polarized source control employed by the HAPPEX experiment at Jefferson Laboratory.

beam entered the polarized source vacuum. It was found that the position differences varied very significantly when the orientation of the half-wave plate was varied azimuthally with respect to the laser beam path. Empirically, an orientation of the half-wave plate was established where the helicity-correlated position shifts were of the order of 200 nm in both dimensions. This procedure maintained the helicity-correlated centroid differences of the electron beam on target to be less than 20 nm.

A schematic diagram of the important components of the HAPPEX experiment that are used to control, monitor and compute systematic helicity-correlated beam fluctuations is shown in Figure 15. For the next generation of experiments, the physics that drives these position fluctuations will have to be much better understood. One possible candidate is a variation of the degree of circular polarization of the laser beam at the face of the Pockels cell. A second possibility is a variation in the analyzing power of the photocathode to linearly polarized light across its face. A third possibility is nonuniformity in the birefringence of optical elements. The reality is likely to be that all the effects are important. Innovative ways will have to be developed to reduce these effects further.

4.7 Targets

Parity violation experiments are typically high luminosity experiments. Further, since the scattered flux is integrated, typically low Z targets have been used in order to reduce the contributions to the scattered flux from complicated background processes. To date, dense cryogenic hydrogen and deuterium targets and solid carbon and beryllium targets have been used. The cryogenic targets have always pushed the limits of technology in terms of luminosity on target [95]. The next generation of experiments all require targets with cooling power of a kilowatt, which is the state of the art in target technology and typically is the limiting constraint in determining the operating design luminosity.

There is one important issue dealing with the stability of the density of a cryogenic target. In

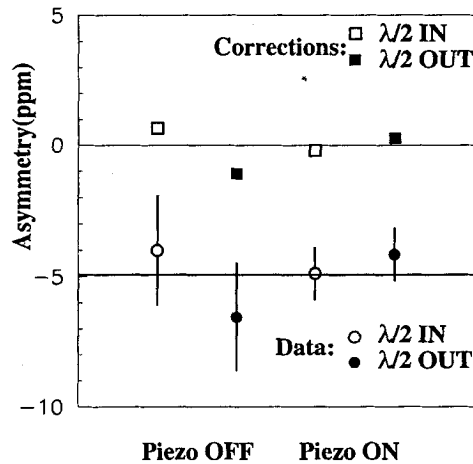


Figure 14: Data from the SAMPLE experiment, together with the size of the corrections due to helicity-correlated beam parameters. The effectiveness of the Piezo-electric feedback is evident.

conventional scattering experiments measuring absolute cross sections, it is important to know the absolute target thickness under running conditions. In parity violation experiments, knowing the absolute thickness is not important. However, random and systematic beam jitter that cause the reduction in absolute thickness may induce density fluctuations that can give rise to dangerous systematic errors.

For example, random jitter in the beam intensity can induce random jitter in the effective thickness of a cryogenic target due to the varying heat load. The net effect is a small quadratic dependence on the beam intensity. Depending on the size of the density fluctuations, the fluctuations in the integrated scattered flux could potentially be degraded significantly, thus effectively increasing the running time. Another very serious source of potential systematic error is a helicity correlated fluctuation in the width of the electron beam at the target. This would effectively induce a helicity correlated target density

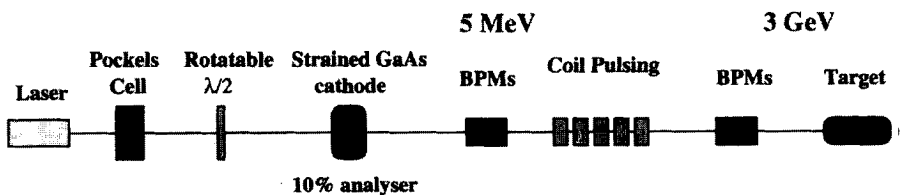


Figure 15: The main components relevant for the control, monitoring and computation of corrections of helicity-correlated beam motion is shown for the HAPPEX experiment at Jefferson Laboratory.

fluctuation that is extremely hard to evaluate and control.

4.7.1 Measurements of Density Fluctuations

It is important therefore to ensure that all sources of target density fluctuations are much smaller than the anticipated statistical fluctuations ($\sigma(A_i)$). Experimentally, this is verified by varying the luminosity on target in a variety ways, such as beam current, repetition rate, beam pulse width, target pump speed etc.

One way to study this effect is to look at the window-to-window fluctuations in the integrated detector response as a function of incident beam current. Such a test was carried out during the commissioning stages of the HAPPEX experiment. The incident energy was 925 MeV, so that the expected rate at a scattering angle of 12.8° with a 15 cm LH₂ target was between 40 and 50 MHz into each spectrometer for a beam current of 100 μ A. At the maximum current, $\sigma(A_i)$ was therefore expected to be $\sim 4 \times 10^{-4}$.

Figure 16 shows the measured standard deviation in the detector asymmetry for 15 Hz window pairs as a function of beam current. The raster size for all the measurements was 2 mm. The expected dependence of $\sigma(A_i)$ is best seen in a log-log plot. It can be seen that the dependence is nearly linear all the way to 100 μ A. Another way to look at the data closely is to plot the estimated standard deviation

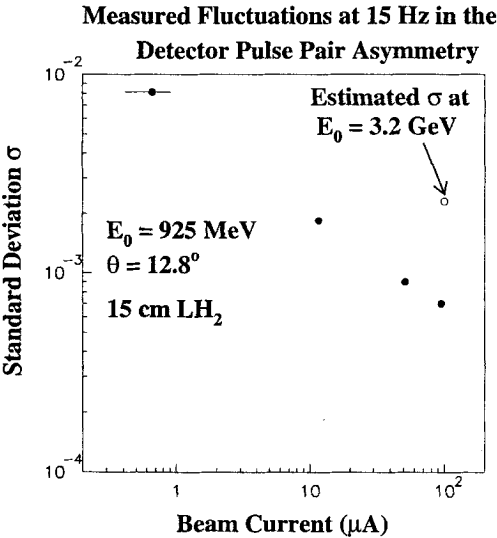


Figure 16: The measured widths of the detector asymmetry integrated at 15 Hz is shown as a function of beam current. Also shown is the estimated width for the kinematics of the physics run in 1998.

tion from each measurement for fixed beam current. Figure 17 shows the data with each measurement extrapolated to reflect the expected fluctuations at a beam current of 100 μ A. If there were no significant density fluctuations, the dependence in this plot should be flat within errors. Clear evidence for

nonstatistical behavior is seen at high current, which we infer to be due to density fluctuations. It is especially suggestive that fluctuations improve with increased raster amplitude.

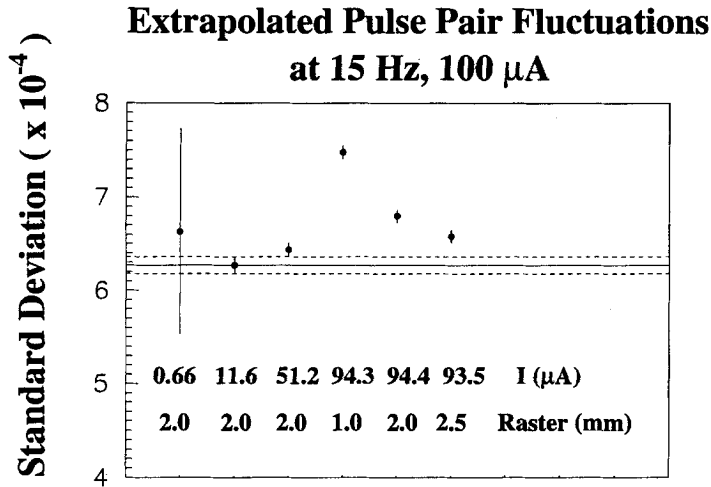


Figure 17: The fluctuations in the integrated detector asymmetry are tested for statistical behavior by extrapolating each measured width to the estimated width at 100 μ A. Clear evidence for additional noise is seen at the highest currents and small raster sizes.

From this data, one can estimate that the amount of boiling with a 2.5 mm raster is about 2×10^{-4} for a 15 Hz window pair. These additional fluctuations are much smaller than $\sigma(A_i)$ for the kinematics of the HAPPEX run (Figure 7). Achieving this goal of reducing the density fluctuations to a negligible level is an important criterion for the running of any parity violation experiment.

4.8 Electron Detection and Measurement

4.8.1 Overview

An important aspect of the experimental design of parity violation experiments is the manner in which a signal proportional to the relative flux of the elastically scattered electrons is generated for the computation of the helicity-dependent cross section asymmetry. Two challenging issues are the very high rates in each helicity window and the rejection of potential prompt and ambient room backgrounds. A third task is to determine the Q^2 of the events with sufficient precision.

In pulsed accelerators, the instantaneous rate is too high to count individual particles in the detector. The detector must therefore produce a direct-current signal that responds linearly to changes in the scattered flux, which can then be integrated over the duration of each helicity window and digitized to obtain a number proportional to the scattered flux. In order for this to work, the detector signal must be dominated by the flux of elastically scattered electrons of interest. This can be accomplished by using a magnetic spectrometer to focus the electrons into a region otherwise free of background as well as by using a detector medium that is sensitive only to the scattered electrons of interest.

The electron detector medium for integrating experiments is usually chosen to be one that is predominantly sensitive to Čerenkov radiation in order to reduce the acceptance of nonrelativistic particles such as neutrons and low energy pions. The Čerenkov radiation is guided into phototubes whose integrated current output provides a measure of the scattered flux. One important issue facing the new generation of experiments is radiation hardness.

The phototube and associated integrating electronics must have sufficient resolution and linearity at very high instantaneous rates. The electronics must be as insensitive as possible to crosstalk from other parts of the experiment in order to preclude the possibility of degrading the counting statistics with random and helicity-correlated pickup.

In CW accelerators, it is possible to contemplate counting individual particles. As we discuss below, this is the method chosen by the G^0 experiment at Jefferson Laboratory and the A4 experiment at Mainz. In both cases, individual particle counting allows online rejection of background particles, which then facilitates having a very large acceptance. These experiments are under construction and will face a series of new challenges as they proceed towards data collection.

We elaborate on the above considerations below.

4.8.2 Magnetic Spectrometers

The most common way to deal with the need to integrate the scattered flux (due to the high instantaneous rates) is to use a magnetic spectrometer system consisting of dipoles and quadrupoles to focus the elastic electrons of interest into a region with very little other background. For example, a magnetic spectrometer system easily allows for shielding from prompt background arising at the target.

At the SLAC E122 experiment, the spectrometer accepted charged particles at a scattering angle of 4° . The active elements were a dipole and 3 quadrupoles arranged in a DQQQ sequence. At the Bates ^{12}C experiment, a pair of quadrupole spectrometers were used, placed symmetrically to pick up elastic electron scatters at a scattering angle of 35° . Collimators at the front and back of the quadrupoles and a lead sheet along the horizontal plane in each quadrupole reduced backgrounds to a negligible level.

At the HAPPEX experiment, the HRS spectrometers in Hall A were used to discriminate elastic scatters from inelastic electrons and other background. The spectrometer consisted of a symmetric pair, each of which consisted of a QQDQ sequence of quadrupoles and a dipole. The hardware resolution of the spectrometer was better than $\delta p/p \sim 0.001$, which ensured that elastic electron-proton scattering events cleanly separated from electrons at π^0 threshold on the focal plane. The detector stack intercepted a 15 cm x 100 cm rectangle on the focal plane which was dominated by elastic electrons and its radiative tail.

Figure 18 demonstrates the advantage of a magnetic spectrometer system in not only reducing the backgrounds to insignificant levels but also in providing a clean method to evaluate the sensitivity of the experimental measurement to inelastic processes. The data shown are from a special study carried out at the kinematics of the HAPPEX experiment, where the response of the detector was measured as the momentum setting of one spectrometer was increased. A powerful demonstration of the cleanliness of the measurement is the fact that measurements with the detector set in integration mode as well as counting mode agree over the full range of energy loss.

When the spectrometer setting is 20% high, the signal is reduced by four orders of magnitude. This demonstrates the excellent shielding from room background. For smaller momentum mismatches the background rejection is less, due to rescattering of inelastic electrons, mostly in the last quadrupole. The signal is still reduced by a factor of 100 at the threshold for neutral pions and a further factor of three on the peak of the delta. The net result was that the backgrounds were measured to be less than 0.2%.

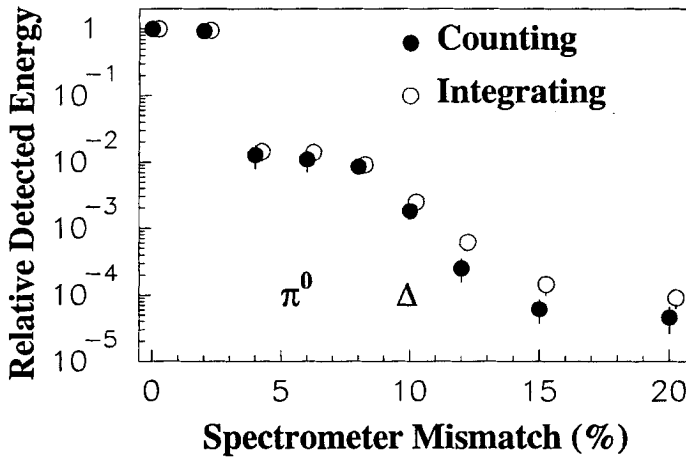


Figure 18: Sensitivity of the HAPPEX detector for inelastic events determined by mistuning the spectrometer. The inelastic threshold, corresponding to π^0 production, occurs for a 5% mismatch. The peak of the Δ -resonance occurs at a 10% mismatch.

The G^0 experiment under construction will use a spectrometer comprised of eight superconducting coils in a toroidal geometry. Recoil protons from the elastic scatters with $\theta_{lab} \sim 87^\circ$ are focused onto a surface. Position along the surface results in a clean Q^2 separation over a total solid angle of 0.9 sr. This geometry provides line-of-sight shielding of the detectors from the target. The recoil protons are separated from background particles using time of flight information.

4.8.3 Options without Magnetic Spectrometers

The kinematics may be chosen with sufficiently low beam energy so that inelastic events in the desired direction are either kinematically forbidden or too low in energy to be detected. Then a technique that provides large solid angle at wide angles is to use the Čerenkov light produced by the scattered particles as they pass through the air. This method was pioneered by the Mainz experiment and is being used by the SAMPLE experiment.

At SAMPLE, the range of scattering angles covered is between 130° and 170° for a total solid angle of 1.5 sr. An array of ten ellipsoidal mirrors focusses the Čerenkov light onto ten eight-inch diameter phototubes. The challenge of the open geometry is to suppress ambient room background. This requires good electron beam quality with minimal halo. Careful monitoring of prompt backgrounds such as pions and muons is also required.

The A4 experiment under construction at Mainz takes a new approach. They plan to build a calorimeter and detect all particles in a range of scattering angles centered around $\theta_{lab} \sim 35^\circ$ in the full range of the azimuth for a total solid angle of 0.7 sr. The calorimeter is designed to detect the

10^7 e^- /s rate from elastic events amongst a background of 10^8 /s. It must reject inelastic events, even those corresponding to single pion production. The collaboration has chosen to solve this problem by using an array of PbF_2 crystals.

4.8.4 Detectors

The detector is designed to produce an output current that is proportional to the scattered electron rate. For the magnetic spectrometers using the integration technique, the detector is typically a total absorption calorimeter that is predominantly sensitive to Čerenkov radiation. SLAC E122 used a lead glass array, while HAPPEX used a sandwich detector made of alternating plates of lead and lucite.

Poor resolution for single electrons in a calorimeter can add significantly to $\sigma(A_i)$, the nominal width of window pairs, and in turn degrade the counting statistics. If $\sigma(E)/E$ is the nominal fractional resolution for a single particle shower and N is the total number of scattered electrons in a single window pair, then

$$\sigma(A_i) = \frac{1}{\sqrt{N}} \left(1 + \left(\frac{\sigma(E)}{E} \right)^2 \right). \quad (70)$$

The detectors are typically optimized to provide better than 20% resolution for single electrons at the nominal scattered electron energy so that the increase in running time to achieve the experimental statistical error is increased by no more than a few percent.

For the new generation of experiments using high rate integration detectors, the radiation damage from the primary scattered flux will be large enough that new materials have to be used for the light sensitive medium. The method of choice, based on detector research carried out for forward angle detectors at the Large Hadron Collider, is to use quartz fibers [97, 96]. The quartz is in reality amorphous silica and can withstand radiation levels of more than 1 GRad. Such a detector is being designed and constructed for use at the E158 experiment at SLAC.

The A4 experiment has chosen an open geometry with no magnetic spectrometer. The calorimeter, therefore, has to have a very fast rise time, with charged particle showers that produce only Čerenkov radiation. It also must be very radiation hard. The solution found is an array of PbF_2 crystals. PbF_2 is intrinsically fast, produces only Čerenkov radiation, and is transparent for light above 270 nm. It can withstand 10 kRad of radiation and be annealed by visible light. The detector is very compact, since the radiation length is 0.9 cm and the Moliere radius is 2.2 cm. The light yield is 1.3 photoelectrons per MeV. The resolution has been measured to be 3.2% at 1 GeV. A spectrum of electrons scattered from a hydrogen target is shown in Figure 19, where elastic peak is clearly visible.

4.8.5 Integrating Electronics

For the parity violation experiments using the flux counting technique, the calorimeter signals as well as the beam monitoring signals have to be processed by a custom-built integrating analog to digital converter (ADC). Such ADCs have kept pace with technology and have evolved considerably since the first parity-violation experiments.

The modern version of the ADC must have true 16 bit resolution, tolerate integration times ranging from 1 μs to 100 ms at repetition rates up to 1 kHz. The differential and integral nonlinearities must be better than 1 part in 10^4 , and the intrinsic pedestal noise must be less than 250 μV . Moreover, the ADC must be insensitive to spurious sources of noise and electronic pickup from the accelerator environment. All parity violation experiments under construction are designing electronics to meet these specifications.

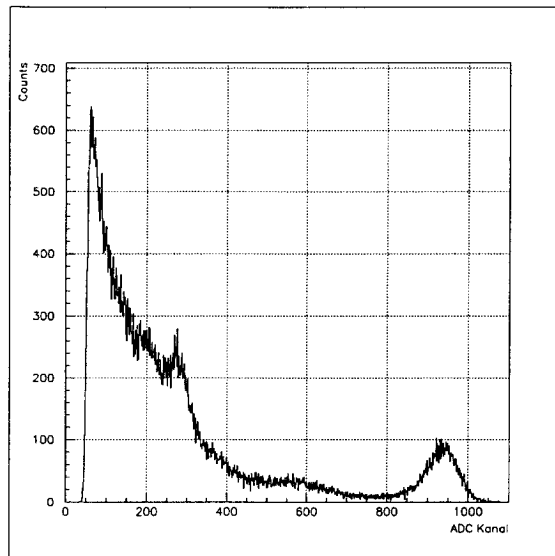


Figure 19: Spectrum of electrons scattered by hydrogen into a PbF calorimeter. The elastic peak is just above channel 900.

As an example, we briefly describe the integrating ADC that was designed for the HAPPEX experiment [98]. A schematic diagram of the main components of the ADC are shown in Fig. 20. Each channel consists of 4 separate components: the integrator, the sample/hold and difference circuit, the DAC summing circuit and the ADC chip. The integrator has less than 100 pA of leakage current and settling time less than 1 μ s. The integrator is sampled between the arrival of two control signals. The two sample/hold circuits hold these levels and feed them into a difference amplifier. The output of the difference amplifier is sent into an analog summing circuit. Here a DC level of a 16 bit DAC compressed by 5 bits is added to the signal. The summed signal is added to the ADC chip.

To demonstrate the performance of the integrating ADC to measure the beam intensity accurately, we show data taken from a test run during the preparations for the HAPPEX experiment. In Fig. 21a, we give the normalized differences between successive measurements (at 60 Hz) of the electron beam intensity. The small width of the distribution demonstrates the remarkable stability of the electron beam at Jlab. In Fig. 21b, we show the residuals from the comparison of two adjacent current monitor difference measurements. The resolution is 50 ppm per sample, adequate for the next generation of parity violation experiments at Jlab.

The integrating ADC was also used in HAPPEX to measure the cross section asymmetry. Again, resolution was a key issue, which was tested during commissioning by comparing the fluctuations in the integrated detector response with beam on and off (with no change in the parameters of the detector). Figure 22 shows the helicity correlated differences in the integrated detector response, with the phototube HV set so that the rate from a 100 μ A beam corresponds to about 50K channels of the ADC. The fluctuations are significantly bigger when the beam is on, suggesting that the integrated phototube

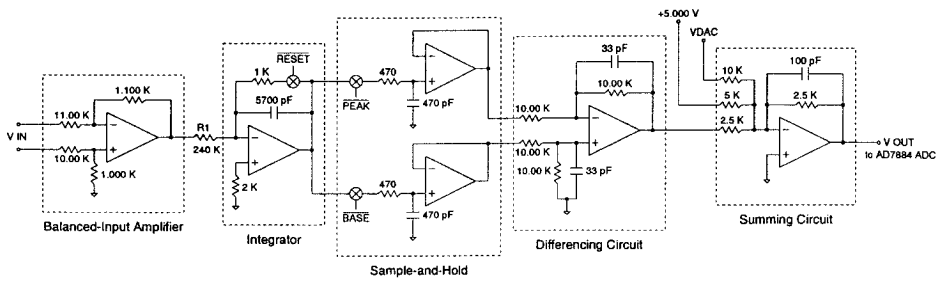


Figure 20: Schematic diagram of the Integrating ADC board.

response is dominated by the statistical fluctuations in the scattered flux.

4.9 Sign Reversals

A fundamental issue in establishing the validity of the measured experimental asymmetry in a parity violation experiment is to demonstrate that the answer is being produced by helicity-dependent dynamics in the cross-section as opposed to a spurious effect in the experimental apparatus. Therefore, it is important to devise methods to reverse the sign of the experimental asymmetry in many different ways which trap for potentially unforeseen classes of systematic effects.

One method used by all experiments is known as “slow helicity reversal”. If circularly polarized laser light traverses a half-wave plate, the emergent light will have the handedness of the circular polarization reversed. This is a powerful technique to trap for spurious effects since the insertion of the half-wave plate is completely independent of the main electronics and data acquisition system of the experiment. Spurious asymmetries generated for example by electronic pickup will not change sign under slow helicity reversal while the physics asymmetry should have equal magnitude and opposite sign under the presence or absence of the half-wave plate.

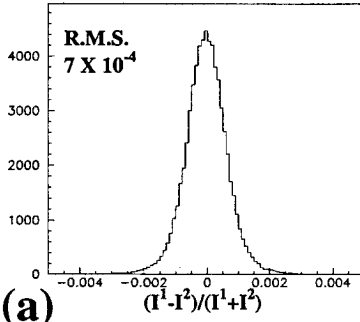
Figure 23 shows data for the HAPPEX experiment with the data sets separated by the presence or absence of the half-wave plate. This procedure of inserting or removing the half-wave plate was typically carried out once a day. The clear correlation between the sign of the experimental asymmetry and the state of the half-wave plate is seen, giving strong confidence that the measured effect is caused by parity violation.

Another powerful method is to use the natural $(g - 2)$ precession of high energy electrons to reverse the sign of the asymmetry. After acceleration to the nominal beam energy, the electron beam is typically bent by a significant angle in order to direct the beam to the target. The beam energy is chosen so the orientation of the spin vector as the beam enters the target is exactly parallel or anti-parallel to the momentum vector. A small change in the beam energy can change the number of precession cycles as the electron goes through the bend by exactly one-half. This would result in reversing the sign of the experimental asymmetry with virtually no other change in the experimental apparatus.

An example of systematic errors that can be trapped in this manner is a potential helicity-dependent change in the beam spot size on target. Again, demonstrating that the magnitude of the measured asymmetry is the same for the two different beam energies is a powerful way to validate the experimental result. This technique was used by the SLAC E122 experiment and is planned for the SLAC E158

Normalized Intensity Differences at 60 Hz

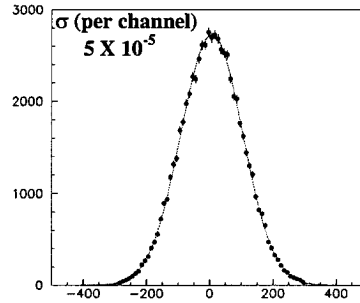
ppm accuracy within few hours



(a)

Current Measurement Resolution

Difference of Current Differences



(b)

Figure 21: Performance of the integrating ADC for the measurement of the beam intensity. The figure on the left shows the normalized differences in beam intensity for successive 60 Hz integrated samples, while the figure on the right shows the residuals from the comparison of measurements from two adjacent current monitors.

experiment.

4.10 Beam Polarimetry

The physics asymmetry A^{PV} is related to the experimental asymmetry A_{exp} by the equation

$$A^{PV} = A_{\text{exp}}/P_e R, \quad (71)$$

where P_e is the measured beam polarization and R includes other normalization factors such as the purity of the signal. Therefore, a crucial part of any parity experiment using polarized electrons is the measurement of P_e .

The first technique used for determining the polarization of an electron beam was Møller scattering [99]. Møller polarimetry has proven to be convenient and has been widely used [100, 101, 102, 103]. With this method, beam electrons are scattered from polarized electrons in a magnetized foil. The useful scattered electrons, which have about half the beam energy and a small scattering angle, can be detected with moderately little background.

For all of the parity-violation experiments presently published, Møller scattering has been one of the primary means for polarimetry. The fractional precision of the measurement of P_e has been on the order of 3–5%, smaller than the fractional statistical error in the parity-violating asymmetry. The relevant sources of systematic error inherent in Møller polarimetry include backgrounds, measurements of the target polarization, the g factor of the electrons in the target, the Levchuk effect [104], rate dependence, and target geometry.

There has been considerable progress over the years in reducing the systematic errors for Møller polarimetry. Recent publications indicate that systematic errors at the 1% level may be achieved [105].

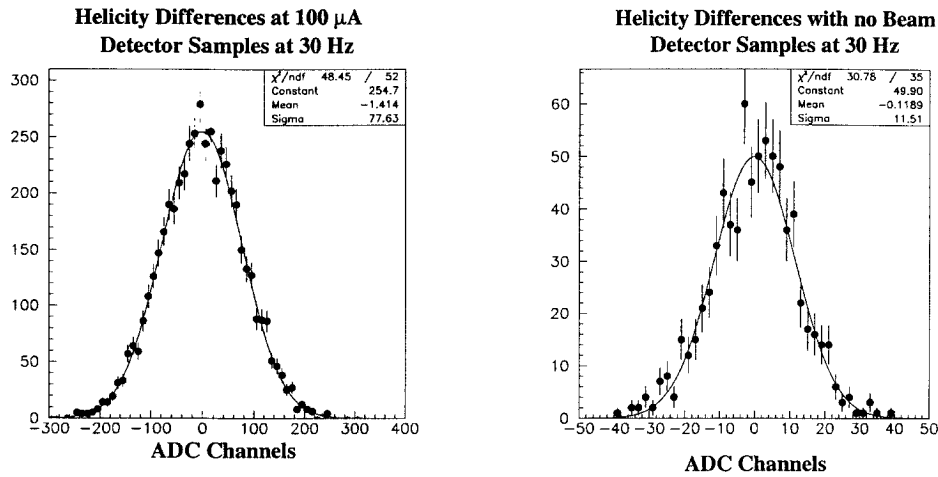


Figure 22: The measured widths of the integrated detector differences for 30 Hz samples are compared when the phototube has been adjusted to provide a signal of 50K ADC channels for a beam current of 100 μA .

106]. Adapting these methods for the high-intensity beams required for parity-violation experiments will require additional effort.

A technique that has been used in numerous high energy physics experiments is to measure the QED asymmetry in the back-scattering of beam electrons off polarized laser photons (Compton polarimetry) [citeWOO96]. A Compton polarimeter has been recently been commissioned in Hall A at JLab which will work for incident electrons in the range of 1 to 4 GeV [108]. This method has successfully served as a check on the Møller polarimetry for the HAPPEX experiment. By the time the proposed new parity violation experiments are taking data, we expect that this technique will greatly reduce the impact of systematic error from beam polarization. An important advantage of the Compton polarimeter is that it can measure the polarization of the full intensity beam simultaneously with the parity data-taking. This technique has the potential to provide systematic errors approaching 1%.

4.11 Summary and Outlook

After twenty-five years of work in the field of parity violating electron scattering, there has been tremendous progress in measuring small asymmetries. As the discussion over this chapter has summarized, the new generation of experiments are gearing up to measure raw asymmetries with systematic errors approaching a few parts per billion. Several of the future parity violation experiments plan to measure asymmetries with fractional errors at least at the 3 to 4% level [86, 87]. These experiments will require impressive control of additional systematic errors including measuring P_e and accurately determining the average Q^2 of the events.

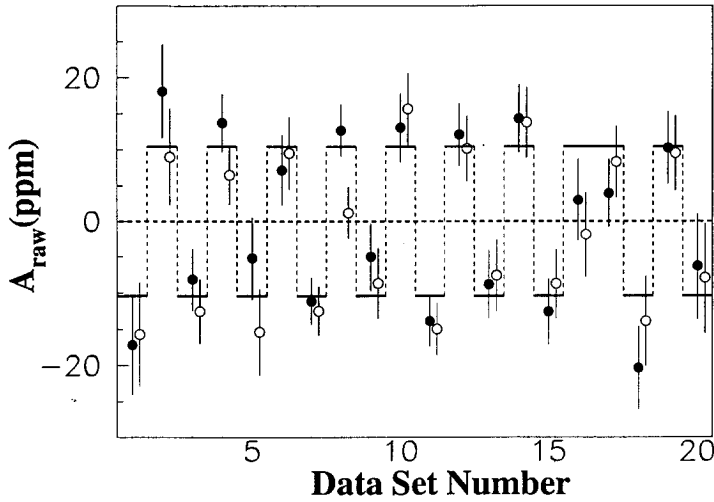


Figure 23: Raw asymmetries as a function of data set for HAPPEX. The sign reverses as expected with the insertion of the half-wave plate. Data from each spectrometer are shown separately.

5 Past and Current Experiments

5.1 Early Electroweak tests

Neutral weak currents, which are now known to be mediated by the Z_0 boson, were first observed in the early 1970's via neutrino scattering. One key issue was whether weak neutral currents violated parity conservation as was the case for the charged weak currents. The neutrino experiments were incapable of addressing this fundamental question. While it was known that the scattering of polarized electrons from unpolarized targets would be sensitive to parity violation, the predicted effects were on the order of 10^{-4} even at $Q^2 = 1(\text{GeV}/c)^2$. Such precision far exceeded that of typical accelerator experiments at that time.

5.1.1 E122 at SLAC

Nevertheless, Prescott *et al.* [75] at SLAC developed an experiment that would measure very small asymmetries. In the process, they developed many of the techniques that are used in many of the parity violation experiments in progress today: a high intensity polarized source, precision beam monitoring

and control, magnetic spectrometer and detector package capable of collecting high statistics.

The reaction chosen was deep inelastic scattering (DIS) from deuterium, which had an asymmetry relatively independent of hadronic structure. Moreover, the accelerator at SLAC was pulsed, producing 2.2 μ sec pulses at 120–180 Hz. With the small duty factor, the rates were so high that individual events could not be counted. Instead the signals were integrated. For DIS in the kinematic region chosen, there is little background, and the rejection of background by coincidence counting methods was unnecessary.

The control of the beam under helicity reversal was impressive by the standards of the day. Energy differences were less than 2 ppm, position differences less than 0.1 μ m, and intensity differences less than 2 ppm. To demonstrate that the small asymmetry measured was indeed parity-violating and not a false asymmetry, two additional methods of helicity reversal were used. One was to rotate a half-wave plate in the laser beam. At one setting, the beam was unaffected. At another, the circular polarization and hence the observed asymmetry was reversed. The other method was to run the experiment at different energies. The helicity of the beam flips 180° for each 3.237 GeV of beam energy in the bend from the accelerator into the experimental hall. Thus, due to this $g - 2$ effect, data at energies that differed by 3.237 GeV should have opposite sign asymmetries.

The asymmetry measured at SLAC showed the proper behavior under reversals, making a convincing case that parity is indeed violated by the neutral weak current. The size of the asymmetry, about 120 ppm when averaged over the various kinematics, was consistent with the prediction of the Standard Model. Finally, the experiment determined that $\sin^2 \theta_W = 0.224 \pm 0.014$.

5.1.2 Quasielastic Scattering off ^9Be at Mainz

At Mainz, a parity experiment was performed that measured a smaller asymmetry of -9.4 ± 1.9 ppm. The experiment was quasi-elastic scattering from Be at an energy of 300 MeV and an angle of 130°. The Mainz experiment pioneered the use of a large air Čerenkov counter to achieve a >2 sr solid angle for the detector. Other innovations included continuous monitoring of the beam polarization by measuring the transmission of photons through magnetized iron.

The interpretation of the experiment is complex since only 59% of the signal came from the desired reaction. Elastic scattering (22%), Δ -resonance (6.5%), and the “dip”-region between the quasi-elastic peak and the Δ (12.5%) also contributed to the signal. Nevertheless, the experiment did set useful limits on any possible anomalous contribution of the axial neutral current of the proton.

5.1.3 Elastic Scattering off ^{12}C at MIT-Bates

At the MIT-Bates Linear Accelerator Center, an experiment that studied elastic scattering from ^{12}C provided another clean test of the Standard Model. The experiment was performed at an energy of 250 MeV and $Q^2 = 0.0225$ (GeV/c) 2 . At this low Q^2 , the contribution of strange quarks is totally negligible compared to the quoted experimental error for any of the models in Table 2. Thus the asymmetry of Eqn. 18 depends only upon the parameters of the Standard Model.

Scattered electrons were detected by a single-quadrupole magnetic spectrometer, which served to reject events that had lost more than 15 MeV. This energy cutoff eliminated uncertainties from poorly understood inelastic nuclear scattering. The experiment consisted of two such spectrometers placed symmetrically in the scattering plane.

One of the challenges of the experiment was the small experimental asymmetry of 0.6 ppm. Thus a number of innovations were required to control the beam under helicity reversal at an unprecedented level. A feedback system was developed to null the helicity-intensity correlation. A system of coils modulated the beam under computer control to measure the sensitivity of the apparatus to beam

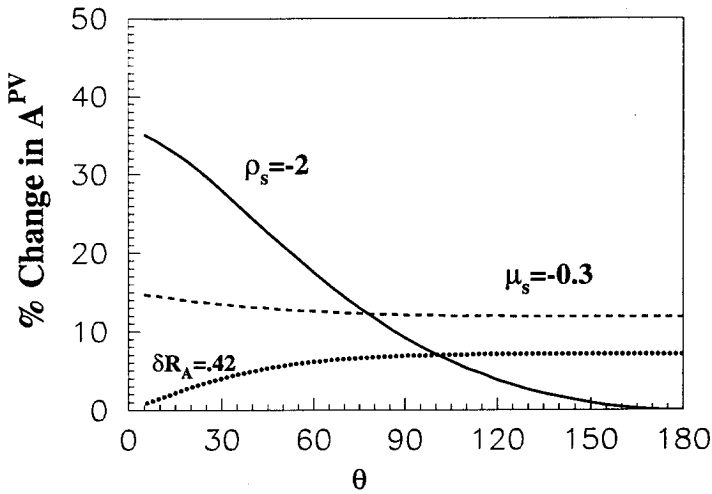


Figure 24: Sensitivity of A^{PV} to strange form factors and the axial radiative correction $R_A^{T=1} \sim -0.42$ at $Q^2 = 0.25(\text{GeV}/c)^2$. We assume $G_E^s(Q^2) = \tau \rho_s G_D$ and $G_M^s(Q^2) = \mu_s G_D$.

position and energy correlations. The estimated contribution of the false asymmetries was on the order of 0.02 ppm. The experiment also featured a high beam current of 30–60 μA . The result was

$$A^{PV} = 1.6 \pm 0.3 \pm 0.1 \text{ ppm}, \quad (72)$$

where the first error is systematic and the second is systematic. This result is in agreement with the prediction of the Standard Model of 1.8 ppm.

5.2 Measurements of Strange Matrix Elements: An Overview

Five experiments in three different laboratories have been approved to measure parity violation in elastic electron-proton scattering. They are listed in Table 6, along with the relevant kinematic parameters. The first goal of the program is to experimentally establish the existence of a nonzero combination of strange form factors. Ultimately, the goal is to measure $G_E^s(Q^2)$ and $G_M^s(Q^2)$ over the range $0 < Q^2 < 1$ $(\text{GeV}/c)^2$. In the process, the program will make significant measurements of the axial strange form factor G_A^s .

5.2.1 Kinematic Coverage and Sensitivity

To understand the motivation of the specific experiments, it is helpful to understand how the sensitivity of A^{PV} to strange form factors varies with Q^2 and θ_{lab} . Also relevant is how experimental uncertainties

Table 6: Kinematics of proton parity-violation experiments. The G^0 has two entries, $G^0(f)$ for forward angles and $G^0(b)$ for backward angles.

Quantity	HAPPEX	HAPPEX II	Mainz A4	$G^0(f)$	$G^0(b)$	SAMPLE
$E(\text{GeV})$	3.3	3.3	0.955	3.0	0.3-0.9	0.20
$Q^2(\text{GeV}/c)^2$	0.48	0.1	0.23	0.16-0.95	0.16-0.95	0.10-0.11
ϵ	0.973	0.994	0.86	0.96	0.17	0.08
$\langle\theta_e\rangle(^{\circ})$	12.5	6	35	5-15	110	135
$A^{PV}(\text{ppm})$	15	6	8	5-30	10-30	7
$\delta A/A_{nom}(\%)$	8	4	5	5	5	14
Particle	e	e	e	p	e	e

as well as uncertainties in the EMFF's affect the interpretation of the results. In full detail, this is a complex question. However, with a few simplifying approximations, we can present a useful general picture.

The first issue is how the experimental error depends on kinematics. As is evident from Table 6, experiments are usually designed to measure the predicted parity violating asymmetry without strange form factors to 5%, regardless of the actual size of the asymmetry. The reason is that various scale errors, such as the beam polarization and the Q^2 of the experiment, tend to enter at that level. Thus the relevant question is how many percent $G_E^s(Q^2)$ and $G_M^s(Q^2)$ contribute to the asymmetry, as well as how uncertainties in the EMFF's influence the interpretation of the measurement. For estimating the required *sensitivities*, the EMFF's may be approximated by the "dipole-Galster" form of Eqn. 40. The vector strange form factors are set to zero, as is the strange axial form factor for the results quoted below. This nominal value for A^{PV} is denoted A_{nom} .

For computing percent sensitivity of A^{PV} to strange quarks, we use $\rho_s = 2$, $\mu_s = 0.3$, assume the form of Eqn. 39 with $\Lambda_{E,M}^s = 0$. This assumption probably overestimates the contribution of strange quarks, especially G_E^s at large Q^2 , but is simple to adjust the result for any Q^2 dependence of the strange form factors. For the uncertainty in the radiative correction, we use the value $R_A^{T=1} = 0.42$. For the EMFF uncertainties, we use 3% errors in G_E^p and G_M^n and a 10% error in G_E^n .

The asymmetry depends on both θ_{lab} and Q^2 . However, the dependence on θ_{lab} is the strongest. In Figure 24 the dependences of the asymmetry on ρ_s , μ_s , and $R_A^{T=1}$ are shown. We chose $Q^2 = 0.25$ as a representative value. From Figure 24, it appears that the most favorable kinematics is for small angles, where ρ_s makes a large contribution but $R_A^{T=1}$ contributes little. Of course, this conclusion comes from the relative size of ρ_s and μ_s , which we have taken from selected models with little justification. If $\rho_s \ll \mu_s$, there is little advantage to forward angles. Furthermore, if the ρ_s and μ_s terms cancel, forward angles are the worst place to look. We note that for the approximation of Eqn. 39, the quantity measured at forward angles is always $\rho_s + \mu_p \mu_s$.

For large angles, the sensitivity to ρ_s rapidly decreases and the sensitivity to the $R_A^{T=1}$ term increases. Then the asymmetry is sensitive to a combination of μ_s and $R_A^{T=1}$. Hence both terms must be measured in a search for strange form factors. One possible method is to measure the asymmetry at *three* different angles. However, there is limited leverage to all three parameters, and the result is that the errors for the individual terms are greatly increased. The alternative method pioneered by the SAMPLE collaboration is to measure the asymmetry for deuterium to independently determine $R_A^{T=1}$.

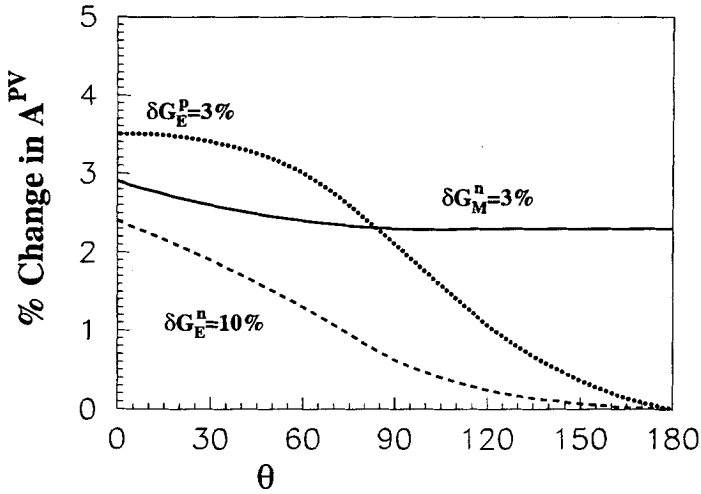


Figure 25: Sensitivity of A^{PV} to errors EMFF's for $Q^2 = 0.25 \text{ (GeV/c)}^2$.

The sensitivity to the EMFF's is shown in Figure 25. For all kinematics, there is significant sensitivity to G_M^n for the simple reason that it is a multiplicative factor in the dominant term in the expression for the parity violating asymmetry. At forward angles, there is significant sensitivity to the other EMFF's. At the present time, improvements in all of the EMFF's would be useful for the determination of the strange form factors.

To illustrate the dependence of the sensitivities on Q^2 , we have plotted in Figure 26 for the G^0 backward angle kinematics ($\theta = 110^\circ$) the contributions to $\delta A/A$ of $R_A^{T=1}$, G_E^p , G_M^n , and $\mu_s = 0.3$ over the range $0.1 < Q^2 < 1 \text{ (GeV/c)}^2$. The changes in sensitivities are small, except for the relatively unimportant G_E^p term. It appears that the sensitivity to μ_s is largest at higher Q^2 values. However, if Λ_M^s is large, the sensitivity would optimize at much lower values of Q^2 . For example, if $\Lambda_M^s = 5$, the sensitivity to μ_s would be reduced by a factor of about 2 at $Q^2 = 0.5 \text{ (GeV/c)}^2$. The sensitivities for the individual experiments are listed in Table 7.

Although many features of these experiments are in common, the detectors are quite different. The solid angle acceptance varies from 0.006 to 1.5 sr. Both counting of individual events and integration are used. Many different detector materials are used. A summary of these characteristics is given in Table 8.

5.3 SAMPLE

The SAMPLE experiment took place at the MIT-Bates Linear Accelerator Center. The goal of the experiment was to measure G_M^s at low Q^2 , which is approximately μ_s , by elastic scattering at backward angles. The kinematics are listed in Table 6. Both hydrogen and deuterium were used as targets.

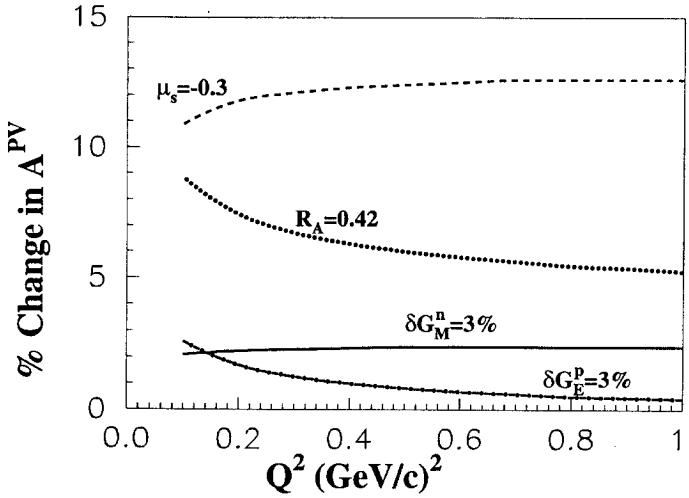


Figure 26: Typical Q^2 dependence of sensitivities of A^{PV} . Here $\theta = 110^\circ$, as is the case for the G^0 experiment at backward angles. We have assumed that $G_M^s = \mu_s G_D$.

Data-taking runs with the proton target took place in 1995, 1996, and 1998. The proton data has been published [109, 78]. In 1999, the final phase with a deuteron target was completed, and preliminary results from the deuterium run have been given at conferences. The deuteron run measured the value of $R_A^{T=1}$, which is interesting in itself and also necessary to interpret the proton data in terms of μ_s .

The experiment was designed as follows. Elastic events were detected by the Čerenkov light produced as they passed through the air, the technique pioneered at Mainz [76]. This type of detector can have a very large solid angle and thick targets to provide high rates. For SAMPLE, about 1.5 sr was covered between 130° and 170° . An array of ten ellipsoidal mirrors focussed the Čerenkov light onto ten eight-inch diameter phototubes. The beam energy of 200 MeV was high enough to provide for a reasonably large asymmetry but low enough so that electrons from inelastic events were below the threshold for producing Čerenkov light in air. Inelastic events with potentially uncertain asymmetries are thus suppressed.

Such an open geometry poses a challenge to shield from several sources of room background. The fraction of the signal due to these backgrounds were measured by two techniques. The first technique was to close a shutter in front of the phototubes to block all light generated in the air. With shutter closed, 23% of the signal remained. A second method was to run with very low beam current so that individual pulses could be studied. Elastic electrons, which generate several photoelectrons, could be distinguished from other processes, such as scintillation light produced by X-rays interacting with the air, which generate only single photoelectrons. About 20% of the signal came from X-rays. Finally, 2% of the signal came from muons decaying in the target, which could be distinguished by the characteristic $2.2\mu\text{sec}$ decay at the end of the beam pulses. The elastic events comprised 55% of the signal. The

Table 7: Sensitivity of experiments to uncertainties in various form factors. Also given is the contribution of the axial term. Entries are percent changes in the asymmetries.

Quantity	HAPPEX	HAPPEX II	Mainz A4	$G^0(f)$	$G^0(b)$	SAMPLE
$3\%G_E^p$	2.9	3.5	3.5	2.8	0.4-1.9	1.5
$3\%G_M^n$	2.8	2.3	2.5	2.8	2.3	2.1
$10\%G_E^n$	1.8	2.3	1.9	1.8	0.2-0.4	0.2
G_A term	4.1	2.5	13	4.5	15	22

Table 8: Characteristics of the proton experiments. The target length is L_t . The background fraction is f_B .

Quantity	HAPPEX	HAPPEX II	Mainz A4	$G^0(f)$	$G^0(b)$	SAMPLE
Detector	Lucite Č	Quartz Č	PbF ₂	Scint.	Scint.	Air Č
$\Omega(\text{sr})$.011	.006	0.7	1	0.5	1.5
$L_t(\text{cm})$	15	15	10	20	20	40
$f_B(\%)$	0.1	0.1	few	few	few	40
$I(\mu\text{A})$	30-100	90	20	40	40	40-60

spectrum was verified by coincidence studies with an NaI detector behind one of the mirrors.

Polarized electrons were produced by a Ti-Sapphire laser shining on a bulk GaAs crystal. The polarization of the beam was $36.4 \pm 1.4\%$ as measured by a Möller polarimeter. The accelerator provided $25\mu\text{sec}$ long pulses at 600 Hz. Due to the high instantaneous rates at normal beam currents, the signals were integrated during the pulses. The target was 40 cm long and was designed to provide a constant density with average beam currents of 40-60 μA [95].

Considerable effort was devoted to providing a beam with parameters uncorrelated with helicity. The helicity-correlated intensity difference was nulled with a feedback system that used as its control an additional Pockels cell located between two linear polarizers upstream of the Pockels cell that controlled the beam helicity. This procedure worked well and did not introduce additional unwanted beam correlations. A piezo-driven plate was used to cancel out helicity correlated laser beam centroid differences in the vicinity of the exit face of the Pockels cell [94]. As in the generic experiment, a half-wave plate in the laser beam line was used as an independent reversal.

False asymmetries due to the remaining helicity correlations were removed by a linear regression technique. The method was tested with luminosity monitors located at a scattering angle of 12° . These monitors had superior statistics to the primary detectors and had a known small physics asymmetry. Moreover, they were much more sensitive to helicity correlations in beam parameters such as position and angle. With the piezoelectric feedback off, the luminosity monitors had false asymmetries at the 5 ppm level that were corrected to below 1 ppm with the regression technique. With the piezoelectric feedback on, the asymmetry averaged over both half-wave plate settings was below 0.2 ppm, although for some data sets statistically significant asymmetries at the 0.5 ppm level were observed.

The backgrounds, which arise from processes with small Q^2 , are expected to have negligible asym-

Table 9: Systematic errors for the SAMPLE experiment. The top two entries are estimates of false asymmetries. The latter three entries are scale factors to convert the raw asymmetry to the physics asymmetry.

Source	$\delta A/A(\%)$
Asymmetry	
Shutter closed	13
Beam monitors	5
Scale factors	
R_{el}	4
P_e	4
EMFF's	3
total	15

metries. However, as a check, substantial data were obtained with the shutter closed. The result was that the background corresponding to average of all the mirrors for the shutter closed data contributed -0.57 ± 0.64 ppm to the asymmetry, consistent with the assumption of zero. However, the asymmetries from the individual mirrors were somewhat inconsistent. To include the possibility that this was due to some unknown systematic effect, the authors chose to assume the background asymmetry was zero but assigned an additional systematic error of 0.64 ppm to the final result. A summary of all the systematic errors is presented in Table 9.

The physics asymmetry A^{PV} is related to the experimental asymmetry A_{exp} by the equation $A^{PV} = A_{exp}(R_{el}R_{\gamma}P_e)^{-1}$ where $R_{el} = .55$ is the fraction of the signal coming from elastic events as described above, $f_{\gamma} = 0.86$ is a reduction factor due to bremsstrahlung, and P_e is the beam polarization. Thus the experimental asymmetry is a factor of about 6 smaller than A^{PV} or just below 1 ppm.

The average asymmetry is

$$A^{PV} = (-4.92 \pm 0.61 \pm 0.73) \text{ ppm}, \tag{73}$$

where the first error is statistical and the latter systematic. The theoretical asymmetry is given by

$$A_{th} = (-5.61 + 3.49G_M^s + 1.55G_A^Z) \text{ ppm} = (-5.61 + 3.49G_M^s + 20.6\Lambda_Z) \text{ ppm} \tag{74}$$

The physics implications will be discussed in Sec. 6.

5.4 HAPPEX

The HAPPEX experiment took data in Hall A at JLab in 1998 and 1999. The CW beam of about 3.3 GeV struck a 15-cm long liquid hydrogen target. Scattered electrons were detected by a pair of 5.5 msr precision spectrometers.

The heart of the HAPPEX experiment is the spectrometers, which proved ideal for parity experiments that integrate the signals from the detectors. In particular, the optics provides for a mass focus that physically separates elastic events from all inelastic events. Moreover, when positioned at the most forward angle of 12.5°, the solid angle is a significant fraction of the full range in the azimuth.

The detector was a sandwich of five lead and lucite layers viewed by a single phototube. The detector response depended slightly on the distance to the phototube. This effect was measured during

Table 10: Corrections to the asymmetry and sizes of systematic errors in percent for the measured asymmetry.

Source	Correction	$\delta A/A(\%):1998$	$\delta A/A(\%):1999$
Statistics	—	13.3	7.2
P_e	—	7.0	3.2
Q^2	—	1.8	1.8
Backgrounds	1.2	0.6	0.6

low intensity running with a data acquisition system that recorded individual event triggers. The trigger data was also used to measure the average Q^2 value of the data, corrected for the response of the detector. The overall uncertainty in the Q^2 value was 1.2%, dominated by uncertainties in the survey. Separate low rate runs established that backgrounds were negligible.

The polarized beam took advantage of many of the techniques described above. Due to the CW nature of the beam, the frequency for helicity flipping could be arbitrarily chosen. The helicity was set every 1/30 of a second (locked to the AC line frequency), and the data were integrated over 32 ms “windows,” allowing time for the voltage in the pockels cell to stabilize. For the even windows, the helicity was randomly chosen, and the complement was used for the odd windows. Thus, each pair of windows comprised an individual measurement of the asymmetry.

As discussed earlier, the raw asymmetry for pairs of opposite helicity windows during the entire run is plotted in Figure 7 and shows that the raw asymmetry distribution is gaussian over 6 orders of magnitude.

One important systematic test involves the insertion of a $\lambda/2$ plate in the laser beam striking the cathode to reverse the sign of the raw asymmetry. The data were divided into sets of about 24 hours duration after which the status of the $\lambda/2$ plate was reversed. The results for the 1999 data are shown in Figure 23. The signal is seen to reverse sign as expected.

The main difference between the 1998 and 1999 running was the nature of the polarized beam. In 1998, a bulk GaAs crystal produced about $100\mu\text{A}$ of 39% polarized beam. The quality was excellent. Helicity-correlated position differences were on the order of a few nm! A total of 85C of charge was collected. For the 1999 run, a new strained GaAs cathode produced 70% polarized electrons. The intensity was lower, about $35\mu\text{A}$. Nevertheless, about 75C of beam was accumulated, and the statistical error of the full run was less than half of that of the 1998 data.

To convert the raw asymmetry to the measured asymmetry, the polarization of the beam must be measured. Three methods were used. The first was Mott scattering in the 5 MeV region of the accelerator. This was the main method for the 1998 running. The estimated precision was about 7%. For the 1999 running a Møller polarimeter in the Hall A beam line was the primary monitor. For some data in 1998, the Møller polarimeter served as a check of the Mott data. For the 1999 run, the Møller data, with a 3.2% uncertainty, was the most reliable. During the 1999 run, a laser-Compton polarimeter was commissioned. In contrast to the Møller apparatus, which involved inserting a target and retuning the beam, the Compton apparatus operated concurrently with the HAPPEX experiment. The data were of sufficient quality to demonstrate that no significant changes in polarization occurred between Møller runs.

The final systematic error arose from the determination of the Q^2 of the detected events. Data were obtained with low beam rate and a triggered DAQ to measure the response of the detector as a function

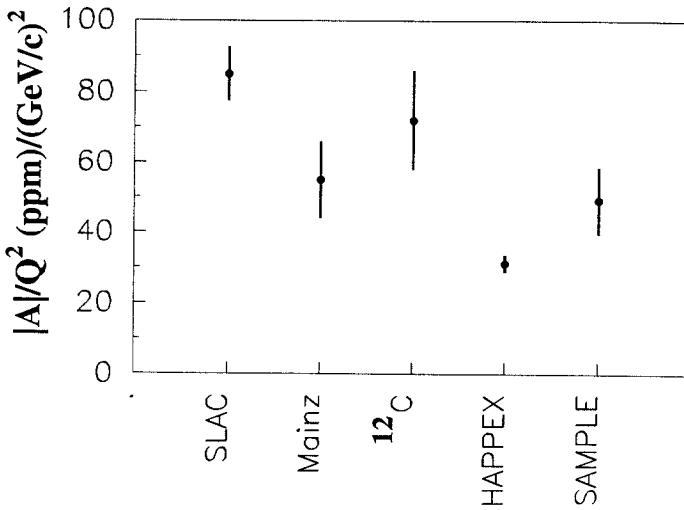


Figure 27: Values of $|A/Q^2|$ for all published parity experiments with polarized electrons.

of the Q^2 of each event. In that way, the correctly weighted average Q^2 was obtained. The dominant errors arose from errors in the survey that determined the angle of the central ray in the spectrometer. The 1.2% error in Q^2 translates to a 1.8% error in the measured asymmetry. The errors are summarized in Table 10.

The result of the 1998 and 1999 data combined is

$$A^{PV} = -14.60 \pm 0.94(stat) \pm 0.54(syst) \text{ ppm} \quad (75)$$

at the average kinematics $Q^2=0.477 \text{ (GeV/c)}^2$ and $\theta = 12.3^\circ$. The asymmetry increased by 0.07% because of the summing over the finite solid angle. The interpretation of this result is given in the next section.

6 Implications of Recent Results

To date, five results on parity violation in electron scattering have been published. The Q^2 values have varied from 0.02–1.4 $(\text{GeV/c})^2$, and the asymmetries have varied from 2–100 ppm. An instructive way to study the results as a whole, suggested by Eqn. 18, is to plot $|A/Q^2|$ for each experiment, as is done in Figure 27. In some general sense, the smaller the error bar on this plot, the greater sensitivity to new physics. By this criteria, HAPPEX is presently the most sensitive experiment.

On the other hand, the sensitivity of A/Q^2 for any given experiment to some particular new physics may depend greatly on the particular kinematics. This is particularly true when using Eqn. 34 to search for the strange matrix elements G_E^s and G_M^s . For simplicity, we will use the parameterization for

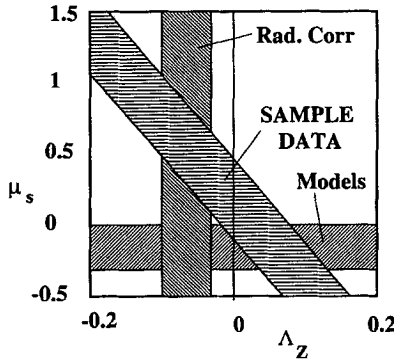


Figure 28: Diagonal band is the data from SAMPLE. The horizontal line covers an expected range for μ_s of 0 to -0.3. The vertical line is the prediction for Λ_Z from Eqn. 60.

the form factors of Eqn. 39 for this discussion. At a given value for Q^2 , the relative sizes of ρ_s and μ_s influence whether forward or backward angles are most sensitive as illustrated for $Q^2 = 0.25 \text{ (GeV/c)}^2$ in Fig 24. The sizes of λ_E^s and λ_M^s strongly determine the optimal Q^2 . Thus, the SAMPLE kinematics are optimal if μ_s is large even if λ_M^s and λ_E^s are larger than 5. The HAPPEX experiment is especially sensitive if ρ_s is large and λ_E^s is much smaller than 5.

If the radiative corrections to the proton axial current are as suggested by Ref. [64, 19], SAMPLE gives the surprising result [78]

$$\mu_s = 0.61 \pm 0.17 \pm 0.21 \pm 0.19, \quad (76)$$

where the first error is statistical, the second systematic, and the third theoretical. This result is of the opposite sign predicted by most models and is quite large if it is not a statistical fluctuation. If the updated numbers from Ref. [67] and Eqn. 60 for the “anapole” correction are used, the SAMPLE result can be plotted as shown in Figure 28.

Preliminary results from quasielastic scattering from deuterium by the SAMPLE collaboration have been reported at conferences [67]. That measurement is much less sensitive to μ_s , and thus can shed light on the result for the proton. In fact, the new deuteron experiment, which has similar errors to the proton experiment, has been interpreted to suggest that the problem may indeed be the prediction for Λ_Z . Experiments with smaller errors are needed, however, to conclusively reject the present calculations.

Naively, the notion that a radiative correction can change a result by 30% is quite surprising in light of the successes in calculating corrections for other processes. One possible explanation is that there is a problem with the anapole moment, which is a set of radiative corrections that does not influence most other measurements. Improved data in the field of parity violation in the interactions of hadrons might reveal parity-violating meson-nucleon couplings larger than assumed in the calculations. Another possibility is significant contributions the box diagrams (see Figure 5 c)) involving two different quarks in the proton. If these diagrams are significant, similar effects might be relevant to many other experiments. The SAMPLE data is causing a careful re-examination of the electroweak radiative corrections.

To determine the strange form factors from the HAPPEX asymmetry, we need values for the EMFF's. At the Q^2 of the HAPPEX experiment, the authors chose $G_E^p/(G_M^p/\mu_p) = 0.99 \pm 0.02$, $G_E^n/(G_M^n/\mu_p) = 0.16 \pm 0.03$, and $(G_M^n/\mu_n)/(G_M^p/\mu_p) = 1.05 \pm 0.02$, which are consistent with the data in Figs. 1 - 4.

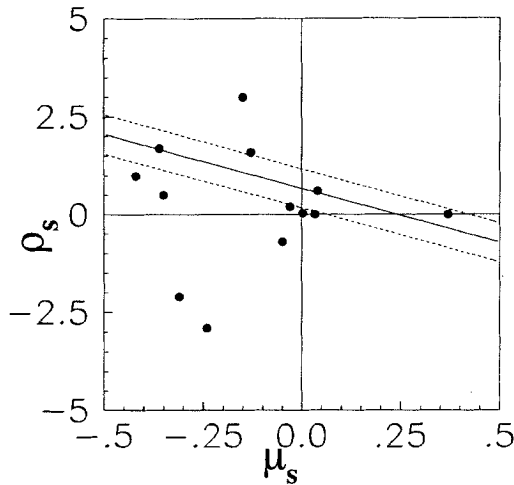


Figure 29: The band gives the result of HAPPEX under the assumption that $\lambda_E^s = \lambda_M^s = 0$. Points are theoretical estimates from Table 2.

The contribution of the axial proton term to A_{exp} , based on Eqn. 60, is $A_A = (0.56 \pm 0.23)$ ppm. Then with Eqn. 34, the result is

$$(G_E^s + 0.392G_M^s)/(G_M^{p\gamma}/\mu_p) = 0.091 \pm 0.054 \pm 0.039, \quad (77)$$

where the first error is experimental, including statistical and systematic errors added in quadrature, and the second arises from the form factors. If the result from SAMPLE is used to estimate Λ_Z assuming that the value varies with Q^2 as G_A^D , the central value decreases by about 0.04. The result is consistent with the absence of strange form factors.

The results are quite sensitive to the EMFF's. As an example, if the data from Ref. [46] were used, the result would be $(G_E^s + 0.392G_M^s)/(G_M^{p\gamma}/\mu_p) = 0.143 \pm 0.054 \pm 0.047$. This value would suggest that the strange form factors are nonzero, especially if the errors in the EMFF's were negligible.

To confront the models with the HAPPEX data, some assumption about the Q^2 dependence of the strange form factors must be made. The simplest assumption is that in Eqn. 39, λ_E^s and Λ_M^s are both negligible. Then

$$\rho_s + 2.9\mu_s = 0.67 \pm 0.41 \pm 0.30. \quad (78)$$

This is plotted as a band in Figure 29. Although the result is quite restrictive, there are models with significant strange form factors that are consistent with the data. If the strange form factors drop rapidly with Q^2 , the HAPPEX results could be a factor of two or less sensitive than shown in the figure.

From the data available to date, we conclude the following:

- SAMPLE and HAPPEX have reported significant measurements of the asymmetry for the proton.
- Significant limits on strange form factors have been set.

- Improvements in the data on EMFF's, some of which are in progress, are crucial to the development of the field.
- A careful look needs to be taken of the axial radiative corrections. Are box diagrams important? Are there unexpectedly large parity-violating hadronic couplings present that contribute to the "anapole" moment?
- Additional data on parity violation in electron scattering with smaller errors and a wider range of Q^2 will be important.

7 Upcoming Experiments

7.1 HAPPEX II

As a sequel to the HAPPEX measurement, a new experiment, HAPPEX-II [86], has been approved at JLab. The experiment will use the same beam and target configuration of HAPPEX (3.2 GeV incident beam energy on a 15 cm liquid Hydrogen target), but at a scattering angle of $\theta_{\text{lab}} = 6^\circ$, corresponding to an average Q^2 of 0.11 (GeV/c)². The small scattering angle will be achieved with a combination of the HRS high resolution spectrometers in Hall A combined with septum magnets that are planned to be installed in late 2001.

The physics asymmetry is estimated to be 1.7 ppm. With 100 μA beam intensity and a $P_e = 0.75$ (which is the projected performance of the Jlab beam starting in 2001), a statistical error of 4.6% and a projected systematic error of 2.9% can be achieved in 700 hours. The rate of electrons into each spectrometer is 63 MHz. This experiment will thus require improved monitoring and systematic control compared to HAPPEX, which will be developed over the next couple of years. The experiment also requires a new radiation hard calorimeter to handle the high flux of scattered electrons. The method of choice is a copper quartz sandwich, a technology that has been tested for use in forward angle calorimetry at the Large Hadron Collider.

The measurement would access the linear combination $\rho_s + \mu_p\mu_s$ to an accuracy of ± 0.31 , thus providing information on ρ_s even if λ_E^s is fairly large. Figure 30 shows the projected constraint on the $\rho_s - \mu_s$ plane from the measurement. The points are models listed in Table 2.

7.2 G^0 at Jefferson Lab

The G^0 experiment at JLab proposes to make a complete set of measurements for $0.16 < Q^2 < 0.95$ (GeV/c)². It is based on a novel toroidal spectrometer which detects scattered events for $62^\circ < \theta_p < 78^\circ$. When the spectrometer is oriented in the forward direction, protons are detected with kinematics corresponding to $15^\circ < \theta_e < 5^\circ$ and $\epsilon \sim 1$. The entire Q^2 range is obtained simultaneously with an incident beam energy of 3 GeV. In a second phase, the detector will be rotated by 180° and backward electrons will be detected to obtain small ϵ data. Seven different energies between 0.29 and 0.90 GeV will be required to cover the Q^2 range. Finally, a deuterium target will be used to determine $R_A^{T=1}$. The apparatus will be located in Hall C.

The spectrometer is comprised of eight superconducting coils in a common cryostat. With a diameter of 4 m and an operating current of 5 kA, the total stored energy is 6.6 MJ. The superconductor operates at about 50% of its critical current. The $\int B \cdot dl \sim 1.6$ Tesla-m, providing a bend angle between 35° and 87° for the recoil protons. This geometry provides line-of-sight shielding of the detectors from the target. The solid angle of 0.9 sr is defined by collimators at the inner diameter of the coils.

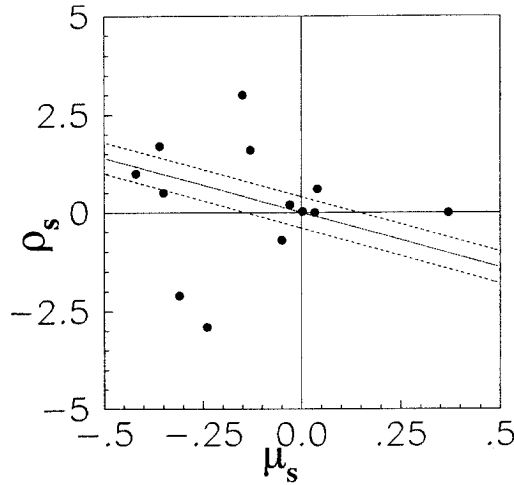


Figure 30: Projected result from the HAPPEX-II measurement. The central value is arbitrarily chosen to go through the origin. The points are theoretical estimates from Table 2.

At the center of the spectrometer is a 20-cm long liquid $\text{H}_2(\text{D}_2)$ target. The key requirement is that the density remain constant despite the deposition of 500W of beam power. These fluctuations must be smaller than the 0.1% statistics obtained during the 30 ms window between beam helicity flips. Based on the SAMPLE design [95], the target features a high longitudinal flow speed of 5-10 m/s designed to provide excellent mixing by turbulent flow.

Scattered particles are detected by pairs of 1-cm thick plastic scintillators. For each of the eight sectors, there are 15 detector pairs, each corresponding to a different Q^2 value. Each scintillator is shaped specially to collect events with the same Q^2 . The high degree of segmentation keeps the instantaneous rates below 1MHz. For forward events, time of flight is used to reject background. The accelerator microstructure is reduced from 500 Mhz to ~ 31 Mhz to provide 32 ns timing windows. The relatively slow protons take ~ 15 -20 ns to reach the detectors. For backward kinematics, additional scintillators near the cryostat are added in coincidence to provide energy and angle measurements.

Custom electronics have been developed to meet the unique demands of the experiment. The timing of the events is determined by the difference between a start signal derived from the accelerator and mean timed scintillator signals that have exceeded an appropriate threshold. Data are recorded both by shift registers feeding scalars and by custom time-to-digital converters. For the backward kinematics, programmable logic chips are used to identify elastic events. Kinematics corresponding to the $N - \Delta$ transition [110] as well as elastic scattering will be employed.

Polarized electrons will be provided by a strained GaAs source. The source will be illuminated by a laser pulsed at 31 MHz to provide the time structure required by the experiment. The beam polarization will be measured by a Moller polarimeter with a projected precision of 2%.

Installation of the apparatus is scheduled for the fall of 2001. Commissioning data will be taken

soon after installation. Physics runs are planned for early 2002.

7.3 Mainz A4

The next parity experiment searching for strange matrix elements is the by the Mainz A4 Collaboration. It will measure elastic scattering from hydrogen at $\theta = 35 \pm 5^\circ$ and $Q^2 = 0.23 \text{ (GeV/c)}^2$. For this kinematics, the asymmetry is 8.7 ppm in the absence of strange quarks. The unique feature of this experiment is a 0.7 sr acceptance PbF_2 calorimeter.

The experiment will take place at the 855 MeV Mainz Microtron (MAMI). Polarized electrons will be provided by a strained GaAs crystal that can deliver a beam current of $\sim 20 \mu\text{A}$. The target will be 10 cm of LH_2 or (LD_2). The target has a high flow rate and high turbulence to dissipate the 80 W deposited by the beam. The beam polarization will be measured with a Compton backscattered laser polarimeter. The beam current, position, and angle will be measured with cavities sensitive to the 2.5 GHz RF-structure of the accelerator. Custom 16-bit ADC's have been developed to process these signals. Current and position are controlled by feedback loops. Data are obtained in 20 ms windows locked to the 50 Hz power line frequency. There will be an H_2O Čerenkov luminosity monitor detecting events between 4 and 11 degrees used to normalize the data. This device will reduce noise due to possible target boiling.

The calorimeter is designed to detect the $10^7 \text{ e}^-/\text{s}$ rate from elastic events amongst a background of $10^8/\text{s}$. It must reject inelastic events, even those corresponding to single pion production. The collaboration has chosen to solve this problem by using an array of PbF_2 crystals. The array will consist of 1022 tapered crystals each with a front surface of approximately $25 \times 25 \text{ mm}$ and a rear surface of $30 \times 30 \text{ mm}$. The thickness is 15 radiation lengths. Light from each 3×3 array of crystals is summed, integrated over 20 ns, digitized, and histogrammed by custom electronics. Both spatial and temporal pile-up are rejected. A diagram of the apparatus is given in Figure 31.

The run is planned for 1000 hr with $\sim 10^{14}$ events expected. The projected errors are 3% statistics and 4% systematics. This will yield a measurement of $F_1^s + 0.13F_2^s$ with an absolute error of 0.02. Initial checkout is scheduled for the year 2000.

7.4 Experiments with ^4He

The problem of the uncertainty in the radiative corrections to the axial nucleon current may be completely avoided by scattering from ^4He [18, 19]. The asymmetry, given in Eqn. 37, is only sensitive to G_E^s . An experiment has recently been approved at JLab which is similar to the HAPPEX II experiment except that the target is ^4He [84]. The Q^2 is 0.1 (GeV/c)^2 , where the elastic form factor of He is still substantial. With the spectrometers in Hall A at JLab, elastic events are cleanly separated from the first inelastic events that have lost more than 20 MeV. The goal of the experiment is to measure $\delta A/A$ to $\pm 3\%$, yielding sensitivities similar to that of HAPPEX II. The implications of the result are shown in Figure 32.

Another ^4He parity experiment has been approved at JLab that will run on the second diffraction maximum at $Q^2 = 0.6 \text{ (GeV/c)}^2$ [83]. At this Q^2 , it is possible that the dominant strangeness effect comes from meson exchange currents [18].

7.5 Other Applications of Parity Violation

The technique of scattering polarized electrons from a fixed target to measure the electroweak asymmetry is also planned for experiments with goals different from searching for strange form factors. Two

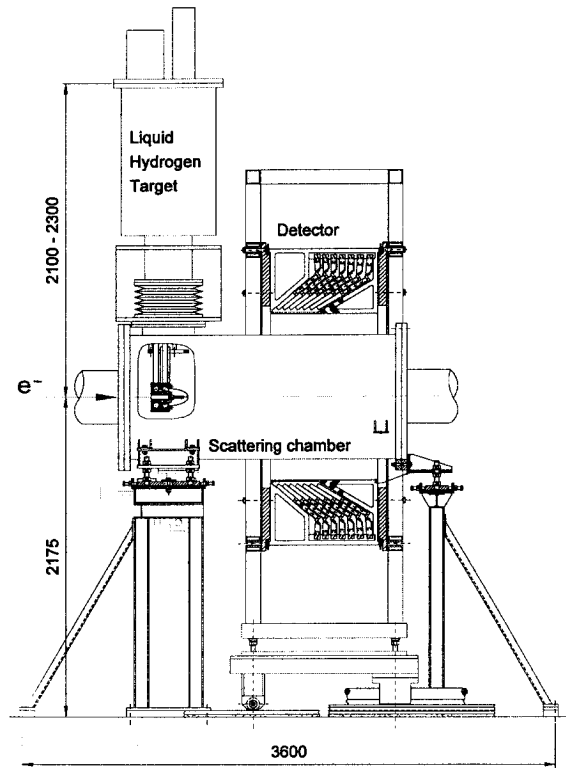


Figure 31: Diagram of the apparatus for the Mainz A4 experiment.

objectives for approved experiments are testing the Standard Model and measuring the radius of the neutron distributions in heavy nuclei.

7.5.1 SLAC E158

Although the Standard Model has been extensively tested at LEP with no conclusive violations, there are still windows for new physics that can be uncovered by low energy experiments. The reason is that new physics at the tree level, such as extra Z' s, new particles such as leptoquarks, or compositeness of leptons or quarks, generate real amplitudes that do not interfere with the imaginary amplitudes on the Z -pole studied at LEP [17, 111].

One such measurement, E158 [85], is scheduled to run at SLAC in the year 2001. The experiment will measure the asymmetry in Møller scattering from the electrons in a hydrogen target. With a beam energy of 48 GeV and a scattering angle of 90° in the center of mass, the Q^2 is 0.02 (GeV/c)^2 . The predicted asymmetry is 0.32 ppm, and the goal of the experiment is to measure $\delta A/A$ to 7%. This precision corresponds to a precision of ± 0.0008 in $\sin^2 \theta_W$. However, $\sin^2 \theta_W$ is expected to vary with

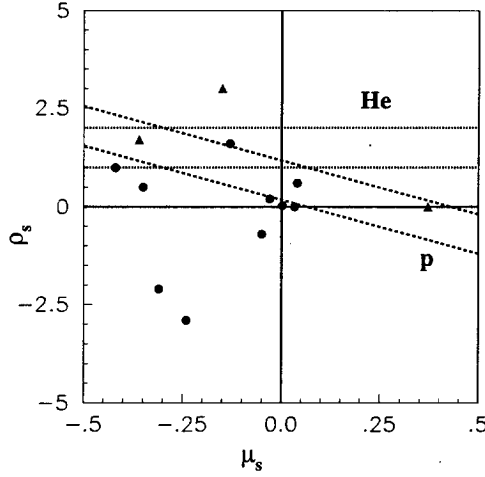


Figure 32: Dotted line is projected result for ${}^4\text{He}$. The central value was arbitrarily chosen to be consistent with HAPPEX, but require a nonzero value for G_E^s . Dashed line is the HAPPEX result as given in Figure 29 for $\lambda_E^s = \lambda_M^s = 0$. Points are theoretical estimates from Table 2.

Q^2 from 0.232 at the Z -pole to 0.238 at the E158 Q^2 [112]. This running of the coupling constant should be clearly seen for the first time. The experiment is sensitive to compositeness of the electron at the 15 TeV scale or new Z -bosons with masses below 1 TeV.

The E158 experiment has a number of unique features. The liquid hydrogen target is 1.5 m long. The scattered electrons are focussed by quadrupoles onto a cylindrical detector. All of the azimuthal solid angle is accepted. About 3×10^7 scattered electrons are detected during each beam pulse. Thus this experiment sets the most stringent requirements in terms of target density fluctuations, beam stability, and radiation hardness of the detector.

7.5.2 JLab ep

Preliminary work has begun on an experimental design at JLab to measure the asymmetry from elastic scattering from hydrogen at an energy of 1.2 GeV and a Q^2 of 0.03 $(\text{GeV}/c)^2$. At these kinematics, the contribution of the strange form factors is small and will be known from numerous experiments. One idea is to reconfigure the G^0 spectrometer to detect electrons at forward angles. The goal of the experiment is to measure $\delta A/A$ to $\pm 3\%$. The experiment could be run at the completion of the G^0 program, which will be after the year 2007.

7.5.3 Neutron Radius of ^{208}Pb

Another approved experiment at JLab is the elastic scattering of polarized electrons from ^{208}Pb [87]. The basic idea is that for electromagnetic scattering, the photon couples to the proton whereas for electroweak interference effects, the Z couples predominately to the neutron [72]. The shapes of the proton distributions of many nuclei have been mapped in great detail with high precision by electron scattering experiments. In the same way, parity-violation experiments can measure the neutron distribution. In practice, only one or two Q^2 points are practical for a parity experiment. However, it is known that proton and neutron distributions have similar shapes, but the average radius of the neutron distribution is probably somewhere between 1–5% larger than that of the proton distribution. Establishing the size of this “neutron skin” at the 1% level is the goal of the JLab experiment, and can be done with a single measurement with minimal theoretical input.

The experiment in Hall A at JLab plans to scatter 850 MeV electrons at 6° . The asymmetry, which is about 0.7 ppm, has been calculated accurately for distorted waves [113]. The goal is to measure $\delta A/A$ to $\pm 3\%$, corresponding to an uncertainty in the neutron distribution radius of $\pm 1\%$. It is interesting to note that the asymmetry for parity-violation in heavy atoms is slightly sensitive to the radius of the neutron distribution, and this experiment may provide relevant input for future, higher precision, measurements with atoms. [114]

8 Conclusions

The field of parity-violation in the scattering of polarized electrons is coming of age. New results are appearing yearly, and the rate of publication is likely to increase. The HAPPEX experiment has set important limits on the presence of strange form factors. The SAMPLE experiment has suggested that the radiative corrections to the proton axial current may be very important.

The new experiments about to take data will clarify the picture. The unexpected effect of the SAMPLE experiment, if as large as suggested, should have a dramatic effects on the new data. With the detailed information available, the source of the discrepancy might be easy to identify. If, on the other hand, the axial corrections are moderate, the new experiments will provide better limits on the strange form factors or even establish their existence.

Finally, new parity experiments will serve to provide even more stringent tests of the Standard Model and also provide a measure of the neutron distribution in heavy nuclei.

Acknowledgments

We would like to thank D. H. Beck, E. J. Beise, C. Cavata, K. de Jager, B. Frois, F. E. Maas, W. J. Marciano, R. D. McKeown, J. Oliver, M. J. Ramsey-Musolf, and C. Y. Prescott. for helpful conversations. This work was supported by the United States Department of Energy under Grant Nos. DE-FG02-84ER40146 and DE-FG02-88ER40415.

References

- [1] J. Ashman *et al.*, *Phys. Lett. B* 206 (1988) 364; *Nucl. Phys. B* 328 (1989) 1.
- [2] D. B. Kaplan and A. Manohar, *Nucl. Phys. B* 310 (1988) 527.
- [3] R. D. McKeown, *Phys. Lett. B* 219 (1989) 140.

- [4] E. J. Beise and R. D. McKeown, *Comments Nucl. Part. Phys.* 20 (1991) 105.
- [5] D. H. Beck, *Phys. Rev. D* 39 (1989) 3248.
- [6] A. O. Bazarko *et al.*, *Z. Phys. C* 65 (1995) 189.
- [7] H. L. Lai *et al.*, *Phys. Rev. D* 55 (1997) 1280.
- [8] B. Borasoy and U.-G. Meissner, *Ann. Phys.*, 254 (1997) 192, and references therein.
- [9] J. Ellis *et al.*, *Phys. Lett. B* 353 (1995) 319.
- [10] K. Abe *et al.*, *Phys. Lett. B* 405 (1997) 180.
- [11] B. Adeva *et al.*, *Phys. Rev. D* 58 (1998) 112002.
- [12] G. Alterelli *et al.*, *Acta Phys. Polon. B* 29 (1998) 1145.
- [13] E. Leader *et al.*, *Phys. Lett. B* 462 (1999) 189.
- [14] H. Lipkin and M. Karliner, *Phys. Lett. B* 461 (1999) 280.
- [15] G. Feinberg, *Phys. Rev. D* 12 (1975) 3575.
- [16] J. D. Walecka, *Nucl. Phys. A* 285 (1977) 349.
- [17] M. J. Ramsey-Musolf, *Phys. Rev. C* 60 (1999) 015501.
- [18] M. J. Musolf, R. Schiavilla, and T. W. Donnelley *Phys. Rev. C* 50 (1994) 2173.
- [19] M. J. Musolf *et al.*, *Phys. Rep.* 239 (1994) 1, and references therein.
- [20] Particle Data Group, C. Caso *et al.*, *Eur. Phys. J. C* 3, 1 (1998).
- [21] E. Hadjimichael, G. I. Poulis, and T. W. Donnelly, *Phys. Rev. C* 45 (1992) 2666.
- [22] G. I. Poulis, *Few Body Systems* 24 (1998) 139.
- [23] R. L. Jaffe, *Phys. Lett. B* 229 (1989) 275.
- [24] H. -W. Hammer, Ulf-G. Meissner, and D. Drechsel, *Phys. Lett. B* 367 (1996) 323.
- [25] W. Koepf, E. M. Henley, and J. S. Pollock, *Phys. Lett. B* 288 (1992) 11.
- [26] M. J. Musolf and M. Burkhardt, *Z. Phys. C* 61 (1994) 433.
- [27] H. Ito, *Phys. Rev. C* 52 (1995) R1750.
- [28] P. Geiger and N. Isgur, *Phys. Rev. D* 55 (1997) 299.
- [29] Ulf-G. Meissner, V. Mull, J. Speth, and J. W. Van Orden, *Phys. Lett. B* 408 (1997) 381.
- [30] B.-Q. Ma, *Phys. Lett. B* 408 (1997) 387.
- [31] H. Weigel *et al.*, *Phys. Lett. B* 353 (1995) 20.
- [32] N. W. Park, J. Schecter, and H. Weigel, *Phys. Rev. D* 43 (1991) 869.
- [33] N. W. Park and H. Weigel, *Nucl. Phys. A* 541 (1992) 453.
- [34] S.-T. Hong, B.-Y. Park, and D.-P. Min, *Phys. Lett. B* 414 (1997) 229.
- [35] S. J. Dong, K. F. Liu, and A. G. Williams, *Phys. Rev. D* 58 (1998) 074504.
- [36] H.-W. Hammer and M. J. Ramsey-Musolf, *Phys. Rev. C* 60 (1999) 045205.
- [37] For a recent discussion of this point, see N. Isgur, *Phys. Rev. Lett.* 83 (1999) 272.
- [38] S. Galster *et al.*, *Nucl. Phys. B* 32 (1971) 221.
- [39] A. I. Akhiezer and M. P. Rekalo, *Sov. J. Part. Nucl.* 3 (1974) 277.
- [40] M. J. Alguard *et al.*, *Phys. Rev. Lett.* 37 (1976) 1258.
- [41] M. K. Jones *et al.*, *Phys. Rev. Lett.* 84 (2000) 1398.
- [42] R. C. Walker *et al.*, *Phys. Rev. D* 49 (1994) 5671.

- [43] G. Hoehler *et al.*, *Nucl. Phys.* B 114 (1976) 505.
- [44] H. Anklin *et al.*, *Phys. Lett.* B 336 (1994) 313.
- [45] H. Anklin *et al.*, *Phys. Lett.* B 428 (1998) 248.
- [46] E. E. W. Bruins *et al.*, *Phys. Rev. Lett.* 75 (1995) 21.
- [47] P. Markowitz *et al.*, *Phys. Rev.* C 48 (1993) R5.
- [48] H. Gao *et al.*, *Phys. Rev.* C 50 (1994) R546.
- [49] S. Platchkov *et al.*, *Nucl. Phys.* A 510 (1990) 740.
- [50] C. Herberg *et al.*, *Eur. Phys. Jour.* A 5 (1999) 131.
- [51] M. Ostrick *et al.*, *Phys. Rev. Lett.* 83 (1999) 276.
- [52] I. Passchier *et al.*, *Phys. Rev. Lett.* 82 (1999) 4988.
- [53] D. Rohe *et al.*, *Phys. Rev. Lett.* 83 (1999) 4257.
- [54] J. Becker *et al.*, *Eur. Phys. Jour.* A 6 (1999) 329.
- [55] W. J. Marciano, *Phys. Rev.* D 20 (1979) 274.
- [56] W. J. Marciano and A. Sirlin, *Phys. Rev. Lett.* 46 (1981) 163.
- [57] A. Sirlin, *Phys. Rev.* D 22 (1980) 971.
- [58] S. Bellucci, M. Lusignoli, and L. Maiani, *Nucl. Phys.* B 189 (1981) 329.
- [59] J. F. Wheeler, *Phys. Lett.* B 105 (1981) 483.
- [60] D. Yu. Bardin, P. Kh. Khristova, and O. M. Fedorenko, *Nucl. Phys.* B 197 (1982) 1.
- [61] M. J. Ramsey-Musolf, private communication.
- [62] W. J. Marciano and A. Sirlin, *Phys. Rev.* D 29 (1984) 75; *Phys. Rev.* D 27 (1983) 552.
- [63] W. C. Haxton, E. M. Henley, and M. J. Musolf, *Phys. Rev. Lett.* 63 (1989) 949.
- [64] M. J. Musolf and B. R. Holstein, *Phys. Lett.* B 242 (1990) 461.
- [65] D. O. Riska, hep-ph/0003132.
- [66] C. M. Maekawa and U. van Kolck, *Phys. Lett.* B 478 (2000) 73.
- [67] S. -L. Zhu, S. J. Puglia, B. R. Holstein, and M. J. Ramsey-Musolf, hep-ph0002252.
- [68] G. T. Garvey, W. C. Lewis, and D. H. White, *Phys. Rev.* C 48 (1993) 761.
- [69] V. Dmitrasinovic and S. J. Pollock, *Phys. Rev.* C 52 (1995) 1061.
- [70] G. A. Miller, *Phys. Rev.* C 57 (1998) 1492.
- [71] R. Lewis and N. Mobed, *Phys. Rev.* D 59 (1999) 073002.
- [72] T. W. Donnelly, J. Dubach, and I. Sick, *Nucl. Phys.* A 503 (1989) 589.
- [73] W. E. Ormand, *Phys. Rev. Lett.* 82 (1999) 1101.
- [74] N. F. Mott, *Proc. Roy. Soc. (London)* A135 (1932) 429; *ibid.* A124 (1929) 425.
- [75] C. Y. Prescott *et al.*, *Phys. Lett.* B 84 (1979) 524.
- [76] W. Heil *et al.*, *Nucl. Phys.* B 327 (1989) 1.
- [77] P. A. Souder *et al.*, *Phys. Rev. Lett.* 65 (1990) 694.
- [78] D. T. Spayde *et al.*, *Phys. Rev. Lett.* 84 (2000) 1106.
- [79] K. Aniol *et al.*, *Phys. Rev. Lett.* 82 (1999) 1096.
- [80] K. Aniol *et al.*, nucl-ex/0006002.
- [81] Mainz proposal A4/1-93 (D. von Harrach, spokesperson).

- [82] JLab experiment 91-017 (D. Beck, spokesperson).
- [83] JLab experiment 91-004 (E. J. Beise, spokesperson).
- [84] JLab experiment 00-114 (D. S. Armstrong and R. Michaels, spokespersons).
- [85] SLAC experiment E158 (K. S. Kumar, spokesperson, E. W. Hughes and P. A. Souder, deputy spokespersons).
- [86] JLab experiment 99-115 (K. S. Kumar and D. Lhuillier, spokespersons).
- [87] JLab experiment 99-012 (R. Michaels and P. A. Souder, spokespersons).
- [88] W. B. Atwood *et al.*, *Phys. Rev. D* 18 (1978) 2223.
- [89] D. T. Pierce and F. Meier, *Phys. Rev. B* 13 (1976) 5484.
- [90] T. Maruyama *et al.*, *Phys. Rev. B* 46 (1992) 4261.
- [91] Z. D. Farkas *et al.*, SLAC PUB 1823, (1976).
- [92] D. H. Whittum and Yu. G. Kolomensky, *Rev. Sci. Instrum.* 70 (1999) 2300.
- [93] P. C. Dunn *Nucl. Instrun. Methods A* A165 (1979) 163.
- [94] T. Averett, C. E. Jones, R. D. McKeown, and M. Pitt, *Nucl. Instrun. Methods A* 438 (1999) 246
- [95] E. J. Beise *et al.*, *Nucl. Instrun. Methods A* 378 (1996) 383.
- [96] N. Akchurin *et al.*, *Nucl. Instrun. Methods A* 399 (1997) 202.
- [97] P. Gorodetzky *et al.*, *Nucl. Instrun. Methods A* 361 (1995) 161.
- [98] J. Oliver, G. W. Miller, and R. Wilson, private communication.
- [99] P. S. Cooper *et al.*, *Phys. Rev. Lett.* 34 (1975) 1589.
- [100] B. Wagner *et al.*, *Nucl. Instrun. Methods A* 294 (1990) 541.
- [101] K. B. Beard *et al.*, *Nucl. Instrun. Methods A* 361 (1995) 46.
- [102] H. R. Band *et al.*, *Nucl. Instrun. Methods A* 400 (1997) 24.
- [103] A. V. Glamazdin *et al.*, *Fizika* B8 (1999) 91.
- [104] L. G. Levchuk, *Nucl. Instrun. Methods A* 345 (1994) 496.
- [105] M. Hauger *et al.*, nucl-ex/9910013.
- [106] D. Adams *et al.*, *Nucl. Instrun. Methods A* 443 (2000) 1.
- [107] See, for example, M. Woods *et al.*, hep-ex/9611005, and references therein.
- [108] D. Neyret *et al.*, *Nucl. Instrun. Methods A* 443 (2000) 231.
- [109] B. Mueller *et al.*, *Phys. Rev. Lett.* 78 (1997) 3824.
- [110] S. P. Wells *et al.*, JLab proposal 97-104.
- [111] K. S. Kumar, E. W. Hughes, R. Holmes, and P. A. Souder, *Mod. Phys. Lett.* A10 (1995) 2979.
- [112] A. Czarnecki and W. J. Marciano, *Phys. Rev. D* 53 (1996) 1066.
- [113] C. J. Horowitz, *Phys. Rev. C* 57 (1998) 3430.
- [114] C. J. Horowitz, S. J. Pollock, P. A. Souder, and R. Michaels, nucl-th/9912038.